



HAL
open science

Experimental investigation of the effect of quenching cycles on the physico-chemical properties of granites

Thomas Junique, Patricia Vazquez, David Benavente, Céline Thomachot-Schneider, Yves Géraud

► To cite this version:

Thomas Junique, Patricia Vazquez, David Benavente, Céline Thomachot-Schneider, Yves Géraud. Experimental investigation of the effect of quenching cycles on the physico-chemical properties of granites. *Geothermics*, 2021, 97, pp.102235. 10.1016/j.geothermics.2021.102235 . hal-03335782

HAL Id: hal-03335782

<https://hal.univ-reims.fr/hal-03335782v1>

Submitted on 16 Oct 2023

HAL is a multi-disciplinary open access archive for the deposit and dissemination of scientific research documents, whether they are published or not. The documents may come from teaching and research institutions in France or abroad, or from public or private research centers.

L'archive ouverte pluridisciplinaire **HAL**, est destinée au dépôt et à la diffusion de documents scientifiques de niveau recherche, publiés ou non, émanant des établissements d'enseignement et de recherche français ou étrangers, des laboratoires publics ou privés.



Distributed under a Creative Commons Attribution - NonCommercial 4.0 International License

1 **Experimental Investigation of the Effect of Quenching Cycles on the Physico-chemical** 2 **Properties of Granites**

3 Thomas Junique¹, Patricia Vazquez¹, David Benavente², Céline Thomachot-Schneider¹, and Yves
4 Géraud³

5
6 ¹GEGENAA EA 3795, University of Reims Champagne-Ardenne, 2, esplanade Roland Garros, 51100
7 Reims, France

8 ²Department of Earth and Environmental Sciences, University of Alicante, 03690 Alicante, Spain

9 ³GeoRessources Laboratory UMR 7359, University of Lorraine, F54505 Vandœuvre-lès-Nancy

10

11 **Abstract:**

12 In this study, the physicochemical properties of granitic rocks subjected to quenching cycles were studied
13 experimentally. Four granites of similar mineralogy but with different degrees of initial weathering (porosity
14 between 1 and 6%) were slowly preheated at two peak temperatures (200 and 400 °C) and then quenched 35
15 times.

16 To study the effect of thermal cycling on the physical properties, non-destructive tests were used such as
17 water porosity, capillary water absorption tests, P- and S- wave propagation velocities, nuclear magnetic
18 resonance relaxometry, and X-ray micro-tomography. Chemical analysis of the granites was performed using
19 X-ray fluorescence, which provided information on the major and trace elements. Water-granite interactions
20 were followed using inductive plasma mass spectrometry (ICP-MS).

21 The variation of all the measured parameters indicates the creation of cracks with thermal fatigue. The
22 porosity, water uptake, size, and volume of cracks increased while P- and S- wave velocity and Young's
23 modulus decreased. At 200 °C, the changes were progressive up to ten cycles, from which the stress threshold
24 was reached and only small readjustments took place. At 400 °C, the greatest damage was observed during the
25 first five cycles. These changes were a direct consequence of the propagation of the microcracks induced by
26 the strong gradient during the quenching tests. For both temperatures, the changes depended on the initial
27 weathering conditions of the granites. Initially, weathered granites showed crack development or crack closure
28 during quenching, meanwhile the damage on the sound rocks was characterized by the creation of
29 intragranular microcracks.

30 The analysis of the experimental fluids showed an enrichment in K, Na and Ca in the solution as consequence
31 of the dissolution of K-feldspar, plagioclase and the degradation of mica and clays, independently of the
32 physical and mechanical modifications.

33

34 **Keywords:** Granites; Thermal cycling; Quenching; Thermal cracking; Microstructural analysis

35 1. Introduction

36 Recent environmental awareness is leading the world towards an ecological transition that requires
37 exploring new renewable energy resources. Among them, geothermal energy is a clean, sustainable
38 energy source with abundant reserves and with enormous potential for electricity generation, but its
39 technical and geological feasibility must be well understood before any production. Enhanced
40 Geothermal Systems (EGS) are man-made reservoirs created by drilling wells in a crystalline massif
41 to access hot rocks in the earth's crust. The injection of cold water into the drilling of the EGS
42 produces an overall rapid cooling of the neighbouring rocks. Hot water vapor reaching the surface
43 turns a turbine to generate electricity. The water after being cooled is returned to the well, which
44 subjects the well to repeated heating-cooling cycles (thermal cycles). These cycles allow to stimulate
45 the geothermal energy reservoir. Thermal stimulation is a reservoir permeability enhancement
46 technique prompted by injecting cold water into a reservoir at high temperature (Flores et al., 2005;
47 Siratovich et al., 2011; Tarasovs and Ghassemi, 2012). The beneficial effect of this process is the
48 initiation and propagation of hydraulic fractures created artificially in rocks of low thermal
49 conduction and composed by minerals with high thermal dilation coefficient, such as granite (Kumari
50 et al., 2018). Fluid flow is improved allowing increased thermal energy production. At the crystal
51 scale, the changes in the geometry of the porous network induced by the mineral shape
52 modification can increase or decrease the flow of fluid in the rock (Takarli and Prince-Agbodjan,
53 2008). The cracks formed in the reservoirs can expand and bring about changes in the physical and
54 mechanical properties of the surrounding rocks. When the crack propagation reaches a certain
55 degree, the stability of the well may change (Bérard and Cornet, 2003; Kumari et al., 2017b;
56 Siratovich et al., 2016). In some areas of a granite reservoir, the thermal gradient can be high and
57 reach $100\text{ °C}\cdot\text{km}^{-1}$ (Baldeyrou-Bailly et al., 2004). EGS are typically systems with temperatures of
58 around 200 °C (Olasolo et al., 2016) although some well temperatures, such as Northwest Geysers
59 (California), are measured at 400 °C . These geothermal systems present a great variety in their
60 environment (temperature, hydrology, geomechanics or petrology) although granite is the primary
61 source rock (Breede et al., 2013). Microcracking can start in granite at around $100\text{-}120\text{ °C}$ (Junique et
62 al., 2021; Lin, 2002) but most mineral crystals are micro-cracked at around 400 °C (Chaki et al.,
63 2008).

64
65 Granite is a low porous and strong material although very sensitive to the effects of temperature.
66 The mineral composition of a granite, the size and grain distribution are major factors that greatly
67 influence mechanical decomposition (Géraud, 1994; Gómez-Heras et al., 2006; Hall and André, 2003;
68 Yilmaz et al., 2009). The increase in temperature will expand the granite minerals. This variation in

69 volume will be different depending on the nature of the grains (Albissin and Sirieys, 1989; Berest and
70 Vouille, 1988). This differential expansion may lead to irreversible microcracks (intergranular and
71 intragranular), generated above a certain temperature threshold (David et al., 1999; Fredrich and
72 Wong, 1986; Junique et al., 2021; Vazquez et al., 2011, 2015). For the most of the studies, the
73 granites were heated to a given temperature although the monitoring experiments were carried out
74 at room temperature after slow cooling down (Chaki et al., 2008; Gautam et al., 2018; Geraud and
75 Gaviglio, 1990; Kant et al., 2017; Reuschlé et al., 2006; Xu et al., 2008). Some studies monitor the
76 possible microcracking during heating by means of acoustic emission or P wave measurements
77 (Glover et al., 1995; Griffiths et al., 2018). In recent years, more researches have been focused on
78 property changes in the rock after experiencing rapid heating-cooling. For example, Pedras Salgadas
79 granite initially heated to 200 °C exhibits a decrease in flexural strength when cooled with water
80 after a cycle (Lam dos Santos et al., 2011). Wu et al. (2019) show that water-cooled samples
81 exhibited a large decrease in P wave velocity and a large number of newly generated cracks on the
82 sample surface. After having subjected a granite to a succession of 20 quenching cycles between 250
83 and 650 °C, it has been shown that the damage, followed by a decrease in the P wave velocity,
84 increased with temperature and thermal shock cycles (Dong et al., 2020). Xu and Sun (2018),
85 reported that wave velocity decreases as the temperature increases for the same quenching cycle
86 and the wave velocity has a weaker relationship for more than five quenching cycles. Li et al. (2020)
87 show on thermal shock cycles that the wave velocity and the elastic modulus decrease with an
88 increase in temperature and that when the temperature is above 300 °C, the pre-existing
89 microcracks expand and eventually develop into larger cracks. Yu et al. (2020) carried out 20 cycles
90 of thermal shock at 300 °C and showed a progressive decrease in the peak strength and elastic
91 modulus with increasing cycles.

92 Water penetrates into the pre-cracked granite through micropores and microcracks, which weakens
93 the cohesive force between the crystals and intensifies the development of cracking (Kumari et al.,
94 2017a). In addition, rapid cooling with water on heat-treated granites induces greater damage than
95 slow cooling, due to thermal gradient cracking (Isaka et al., 2018; Shao et al., 2014). Thus, the
96 permeability of slowly cooled samples increases very weakly at 400 °C, 2.3 times at 500 °C and 35.6
97 times up to 600 °C while the permeability of fast quenching samples increases 2.9 times at 400 °C,
98 15.3 times at 500 °C, or even 79.3 times at 600 °C (Jin et al., 2019). The cracking development during
99 these quenching treatments results in a significant reduction in the strength and elastic parameters
100 of the granite as well as in the physical properties due to an augmentation of crack density (Kumari
101 et al., 2017b; Li et al., 2020). Besides, the effect of cyclic heating-cooling leads to a degradation of

102 rock prompted by the generation and development of micro-cracks (Dong et al., 2020; Kim et al.,
103 2014; Xu and Sun, 2018; Zhu et al., 2020).

104 Geothermal reservoirs present different range of porosity due to damage (microcracks and
105 alteration) (Surma and Geraud, 2003; Zeng et al., 2017) and the role of the initial microstructure on
106 rock cracking is not clear. As a typical heterogeneous material, granites are prone to behave
107 differently depending on their initial state of weathering. Furthermore, the generation of cracks
108 increases the flow performance (Jin et al., 2019; Kumari et al., 2018; Siratovich et al., 2015). An
109 estimate of permeability is therefore essential for applications in the exploitation of unconventional
110 energy and must be correlated with its damage.

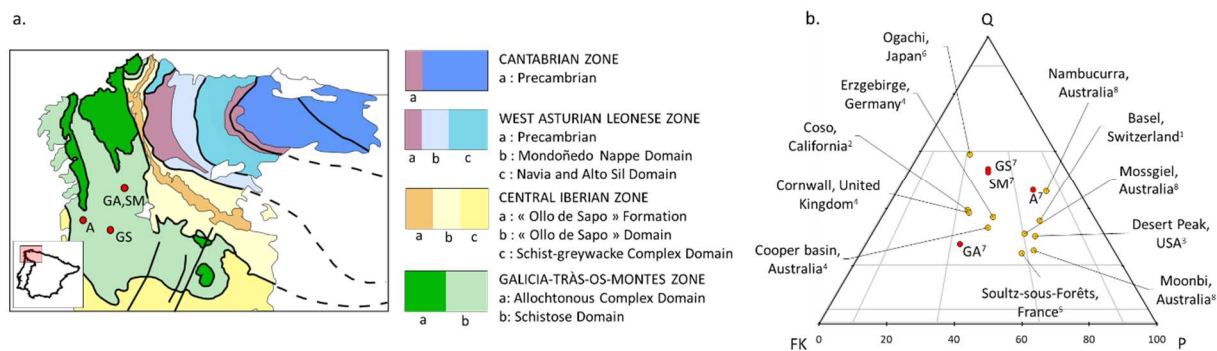
111 Under the thermal effect of quenching, various chemical changes take place in the internal
112 composition of rocks. Many studies in the literature have followed the physical or mechanical
113 properties of granite, however, only a few studies have incorporated the geochemical interaction
114 into the characterisation of cracking processes (Alt-Epping et al., 2013; Baldeyrou-Bailly et al., 2004;
115 Wogelius et al., 2020). Chemical weathering studies after a fluid-rock interaction are often
116 experiments performed on a single mineral phase, and few studies characterise total mineralogical
117 changes in crystalline rocks (Drüppel et al., 2020; Schmidt et al., 2018).

118 The main objective of this study is to evaluate the evolution of the granite's void network when
119 exposed to a succession of quenching and the influence of their initial microstructure. For that, four
120 granites with similar mineralogy but with porosity values between 1 and 6% were tested. To obtain
121 an accurate assessment of the sample evolution, a wide range of non-destructive techniques were
122 used to characterise the microcracking distribution, elastic, mechanical and water transport
123 properties, including water porosity, capillary water absorption tests, ultrasounds, nuclear magnetic
124 resonance (NMR) relaxometry, and X-ray micro-tomography (X-ray CT). Finally, the geochemical
125 interaction between water and minerals after thermal cycling was assessed using inductively
126 coupled plasma mass spectrometry (ICP-MS).

127 2. Materials

128 2.1. Characterisation of the outcrop samples: geological background

129 In this investigation, we selected Albero (A), Gris Alba (GA), Golden Ski (GS), and Silvestre Moreno
130 (SM) granites from the Iberian Peninsula (Fig. 1a) due to their similar mineralogy and crystal size and
131 their difference in alteration degree and porosity. The ternary diagram compares the studied rocks
132 with granites from Enhanced Geothermal System (EGS) around the world (Fig. 1b).



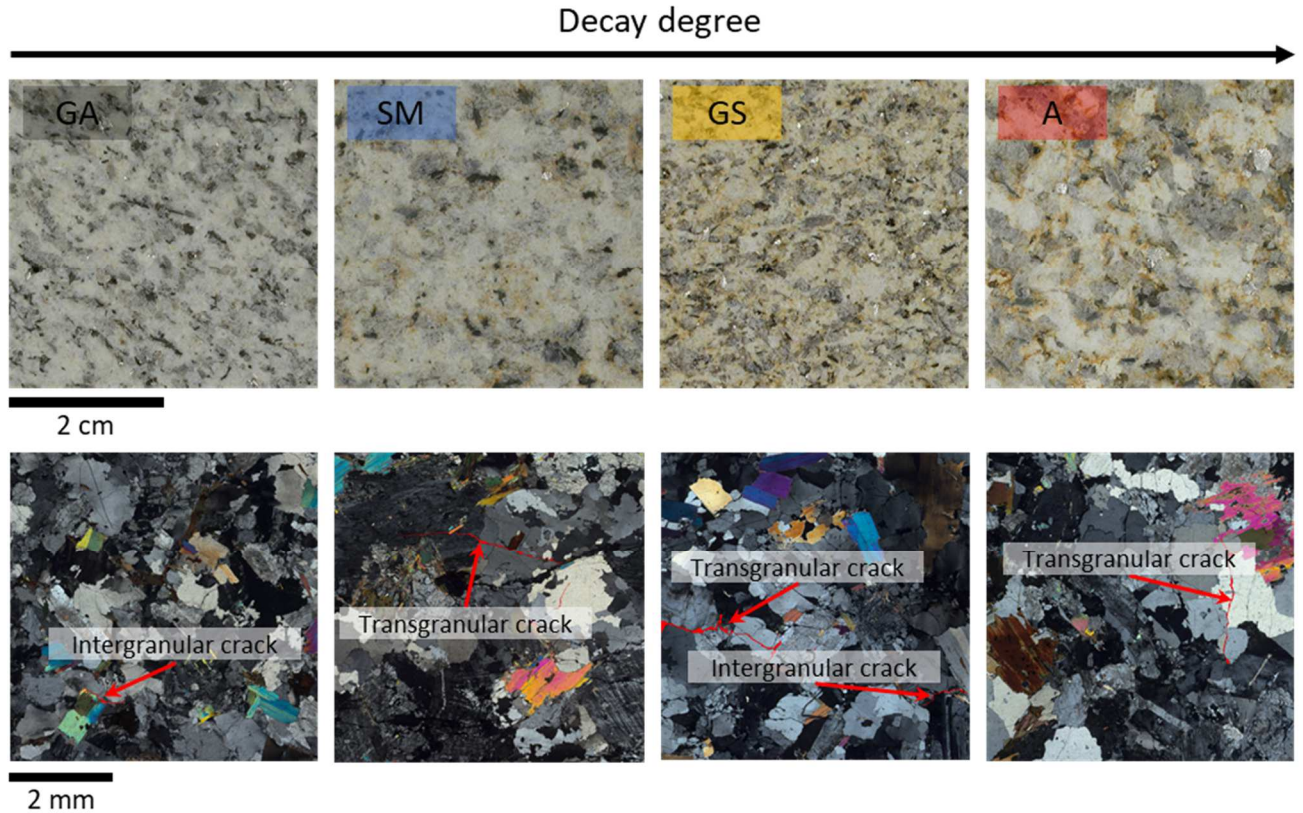
133

134 **Fig. 1: a. Geological and geographical settings of the Iberian granites studied within the diagram of**
 135 **the Macizo Ibérico : Albero (A), Gris Alba (GA), Golden Ski (GS), and Silvestre Moreno (SM)**
 136 **granites. b. Ternary diagram with quartz (Q), potassium feldspar (FK), and plagioclase (P)**
 137 **representing granites of this study (red) and granites from global EGS sites (yellow). (Alt-Epping et**
 138 **al., 2013¹; Kovač et al., 2004²; Lutz et al., 2004³; Marshall et al., 2010⁴; Stussi et al., 2002⁵; Ueda et**
 139 **al., 2005⁶; Vazquez et al., 2018⁷; Zhou et al., 2016⁸).**

140 The granites of this study come from quarries located in the Galician region (north-west of Spain)
 141 and the north of Portugal. The granites are located geologically in the Iberian massif and mostly
 142 structured during the Hercynian Orogenic Belt formation. All the rocks are post-kinematic and syn-
 143 kinematic Hercynian granites and they are located in the so-called Galicia-Trás-Os-Montes area
 144 (Farias et al., 1987). The region is sequentially organised into three groups according to their
 145 compositional characteristics and structural criteria (Vera, 2004): calc-alkaline syn-kinematic
 146 granites, peraluminous syn- and post-kinematic granites, and calc-alkaline post-kinematic granites.
 147 The four studied granites belong to the group of Peraluminous syn and post-kinematic granites. This
 148 group includes granites temporally related to the processes of regional metamorphism and of
 149 Hercynian crustal anatexis. Albero is in Donón-Tomiño alignment which represents an elongated
 150 mass of about 56 km and 12 km wide with a small deformation that gives orientation to the
 151 minerals. This formation of longitudinal axis is parallel to the general directrices of the Hercynian in
 152 this region of Galicia. In 2004, the Geologic and Mining Spanish Institute (IGME) described the Gris
 153 Alba and Silvestre Moreno varieties as "very leucocratic two-mica granites". They are found in the
 154 Salvaterra-A Cañiza-Cerdedo alignment, which belongs to the Faro de Avión batholith. This massive
 155 elliptical shape measures about 7.5 km by 4 km. The Golden Ski variety places within the Salvaterra-
 156 A Cañiza-Cerdedo Alignment, which is an elongated granitic batholith with the longitudinal axis
 157 parallel to the general guidelines of the Hercynian in this area of Galicia.

158 2.2. Granite description

159 Binocular and microscopic views of the studied granites are shown in Figure 2. The petrographic
 160 characterisation (mineral proportion and crystal size) was produced by Vazquez et al. (2018) by
 161 optical polarising microscopy and the main petrographic characteristics are presented in table 1.



162

163 **Fig. 2: Macroscopic and microscopic photography of the studied granite: Gris Alba (GA), Silvestre**
 164 **moreno (SM), Golden ski (GS), and Albero (A).**

165 **Tab. 1: Characteristics of the selected granitoids. Trade name, mineral proportion (studied using**
 166 **optical polarisation microscopy), IUGS classification (Le Maitre, 2002) and the crystal size of the**
 167 **studied granites (Vazquez et al., 2018). (Avg.: Average; Q: quartz; FK: alkali feldspar; P: plagioclase;**
 168 **M: mica).**

Stone	Composition (%)				IUGS classification	Crystal size (mm)				
	Q	FK	P	M		Q	FK	P	M	Avg.
A	35	10	30	25	Granodiorite	5	5	6	4	5
GA	23	37	23	17	Monzogranite	5	5	4	2	4
GS	47	20	20	13	Monzogranite	4	4	4	2	4
SM	45	20	20	15	Monzogranite	4	5	7	4	5

169

170 Albero (A): The yellowish hue found in the granite was due to a notable initial alteration and the
 171 presence of clay. Indeed, this granite was characterised by open transgranular cracks. It was a
 172 homogeneous granodiorite with medium-fine crystal (5 mm). It had the lowest alkali feldspar
 173 content among the four granites studied and a high proportion of muscovite and biotite (25%). A
 174 contains elongated xenomorphic minerals orientated according to the foliation. Most boundaries
 175 were interpenetrated.

176 Gris Alba (GA): The intergranular cracks observed in this granite can be found mainly at the edge of
 177 the micas. It was a homogeneous monzogranite with fine crystal (4mm). It had anhedral minerals

178 and the boundaries between the quartz crystals were irregular. The proportion of muscovite biotite
179 minerals was about 2:1.

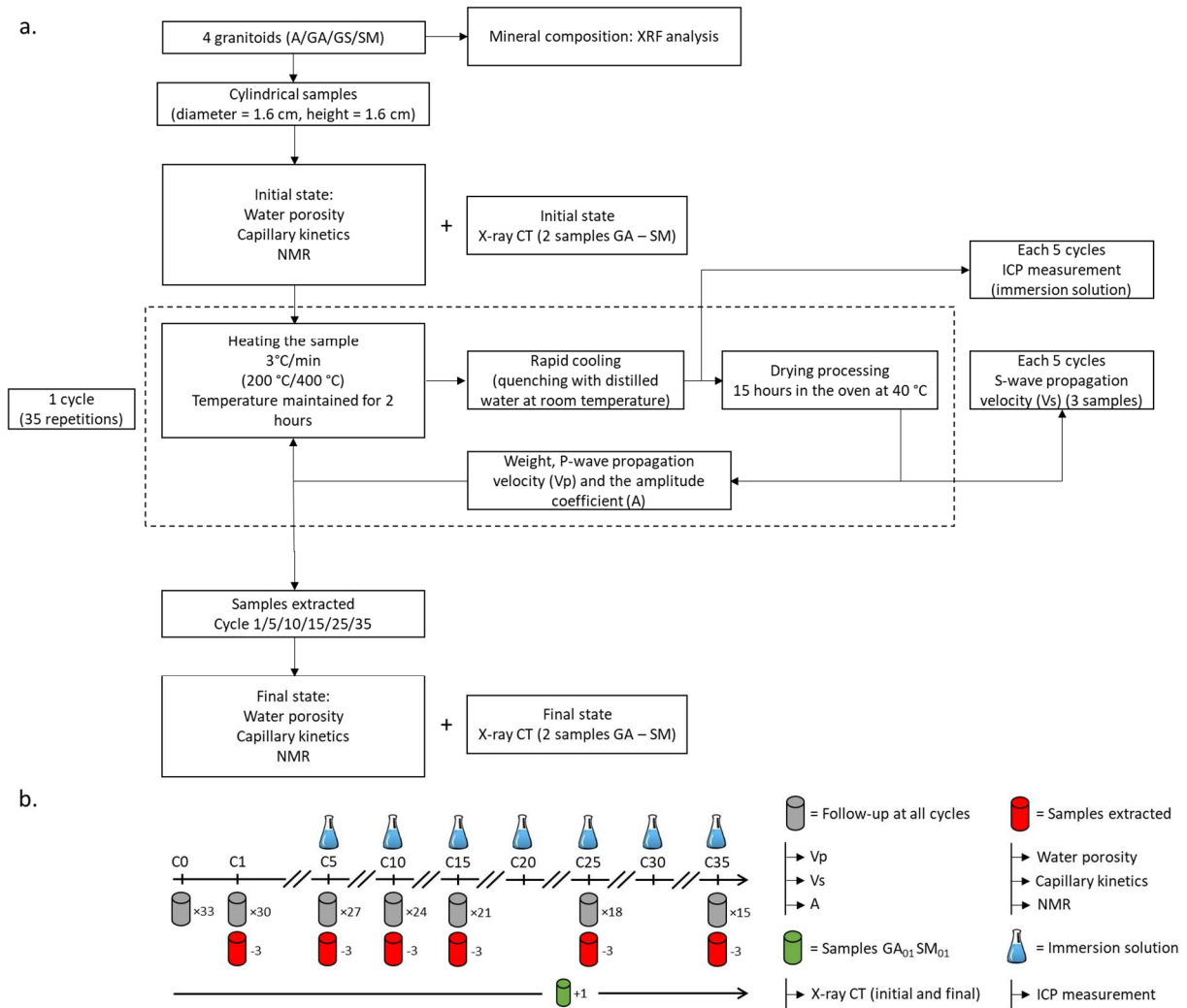
180 Golden Ski (GS): Pre-existing cracks were of intergranular nature and were present in plagioclases.
181 GS also had open transgranular cracks. It was a homogeneous monzogranite with fine crystal (4
182 mm). Quartz and feldspars were subhedral and muscovite was euhedral. These were the muscovite
183 crystals that have the largest crystal size and plagioclase the smallest crystal size. Quartz content was
184 higher than that of feldspars which is 20% of plagioclases. This granite had an initial alteration
185 characterised by the presence of clay.

186 Silvestre Moreno (SM): Like A and GS, this granite had an initial alteration indicated by the presence
187 of intra, inter and transgranular cracks. It was a homogeneous monzogranite of small size (5 mm).
188 These minerals were subidiomorphic. After GS, this granite had the highest quartz proportion of the
189 granitoids studied. SM had the same proportion of feldspars and plagioclase (20%) as GS.
190 Plagioclases were the minerals with the largest size (7 mm).

191 3. Methodology

192 3.1. Sampling and analytical procedure

193 The experimental method was specifically designed to verify the impact of an abrupt change of
194 temperature in the granites (Fig. 3a) because there are not quenching standard tests.



195
196 **Fig. 3: a. Experimental methodology. b. Detail of sampling during the cycles (C).**

197
198 The samples are cylinders 1.6 cm in diameter (d) and 1.6 cm in height (h). A total of 33 samples per
199 granite and per quenching test were used. A total of 3 samples per granite were removed on the
200 1/5/10/15/25/35 cycle for each quenching test. Samples of the purified water (5 ml) used during
201 cooling was removed every 5 cycles for each quenching test (Fig. 3b). The water samples taken will
202 be analysed by inductively coupled plasma mass spectrometry (ICP-MS).

203 3.2. Thermal treatment

204 The main goal was to study the influence of cyclic quenching on the mechanical and microstructural
205 properties of granites. The samples were heated at a rate of 3 °C/min until the target temperature
206 was reached. This heating rate was low enough to avoid thermal shocks on the granite and to ensure
207 that induced microcracks were the direct response of temperature and not of the temperature
208 gradient within the sample (Dwivedi et al., 2008; Li et al., 2020; Zhu et al., 2020). Two heating

209 temperatures (200 and 400 °C) were selected as average and maximum temperatures of existing
210 geothermal systems (Breede et al., 2013). The temperature was kept constant for 2 hours to
211 distribute the assigned temperature evenly (Tang et al., 2019). Cold distilled water (~25 °C) was then
212 instantly inserted into the container containing the samples for 1 hour. This water was changed after
213 each cycle. According to Zhang et al. (2018), the sample surface cooling time was about 10 and 25
214 min for the heating temperature of 200 and 400 °C. This cycle was repeated 35 times.

215 3.3. Physical property tests

216 3.3.1. Water porosity

217 Connected porosity (φ_c) is defined as the ratio of the volume of connected voids to the total volume
218 of rock. In this study, the experimental protocol followed the standard NF EN 1936, (2007). It
219 consists of obtaining the porosity using the triple mass method. The dried samples were weighed
220 and placed in a desiccator where the pressure was gradually lowered with a vacuum pump to
221 remove any air from the pores. The degassed distilled water was then gradually introduced until the
222 samples were completely immersed. Once atmospheric pressure was restored, the samples were
223 left in the water for 24 hours. The saturated mass and the hydrostatic mass of the samples were
224 then recorded.

225 3.3.2. Capillary coefficient

226 Capillarity on a natural stone is an intrinsic property and represents its ability to absorb water under
227 the effect of capillary forces. This property is directly related to the porous network (size, pore
228 shape, and network connection). The capillary coefficient (C) was calculated based on the NF EN
229 1925, (1999) standard. The samples were dried at 40 ± 5 °C before each test until their masses
230 stabilised. The principle of experience is to put our porous solid in contact with distilled water.
231 Capillary kinetics are usually characterised by two phases (Hammecker et al., 1993; Hammecker and
232 Jeannette, 1994). The first phase is the progressive filling of the free porosity by the capillary forces
233 of water without external pressure applied. The slope of this curve represents the capillary
234 coefficient (Roels et al., 2000) that is the volume of water penetrated by capillarity into the rock per
235 unit of square root of time according to the Washburn law ($\text{g}\cdot\text{m}^{-2}\cdot\text{s}^{-1/2}$). The restitution curves of the
236 water uptake tests give information about the porous network (Benavente et al., 2015, 2002). The
237 modification of the porous networks of the samples was only assessed through the variation of this
238 parameter.

239 3.3.3. Elastic rock properties and deduced mechanical properties

240 P- and S-waves propagation velocities (V_p and V_s respectively) were measured to estimate dynamic
241 mechanical rock properties. Moreover, the monitoring of the ultrasonic signal is effective in
242 evaluating the characteristics of the pores of the rock because it depends mainly on the size,
243 connectivity, and distribution of the pores, the lithology, and the bedding plans. Propagation
244 velocities were measured using equipment for receiving non-transmitting signals (Panametrics-NDT
245 5058PR) coupled to an oscilloscope (TDS 3012B-Tektronix). The transducer frequency was centered
246 on 2.5 MHz for P-waves and 1 MHz for S-waves. To ensure the transmission of ultrasonic energy
247 between the transducers and the surface of the sample, a visco-elastic coupler was used. Constant
248 pressure was systematically applied between the transducers and the sample. In this study, the P-
249 wave velocity was measured on all the samples after each cycle of quenching. V_s was measured
250 every 5 cycles on 3 samples for each test.

251 Dynamic Young's Modulus (E) (1) and Poisson's ratio (ν) (2) were calculated as follows (Homand et
252 al., 2000):

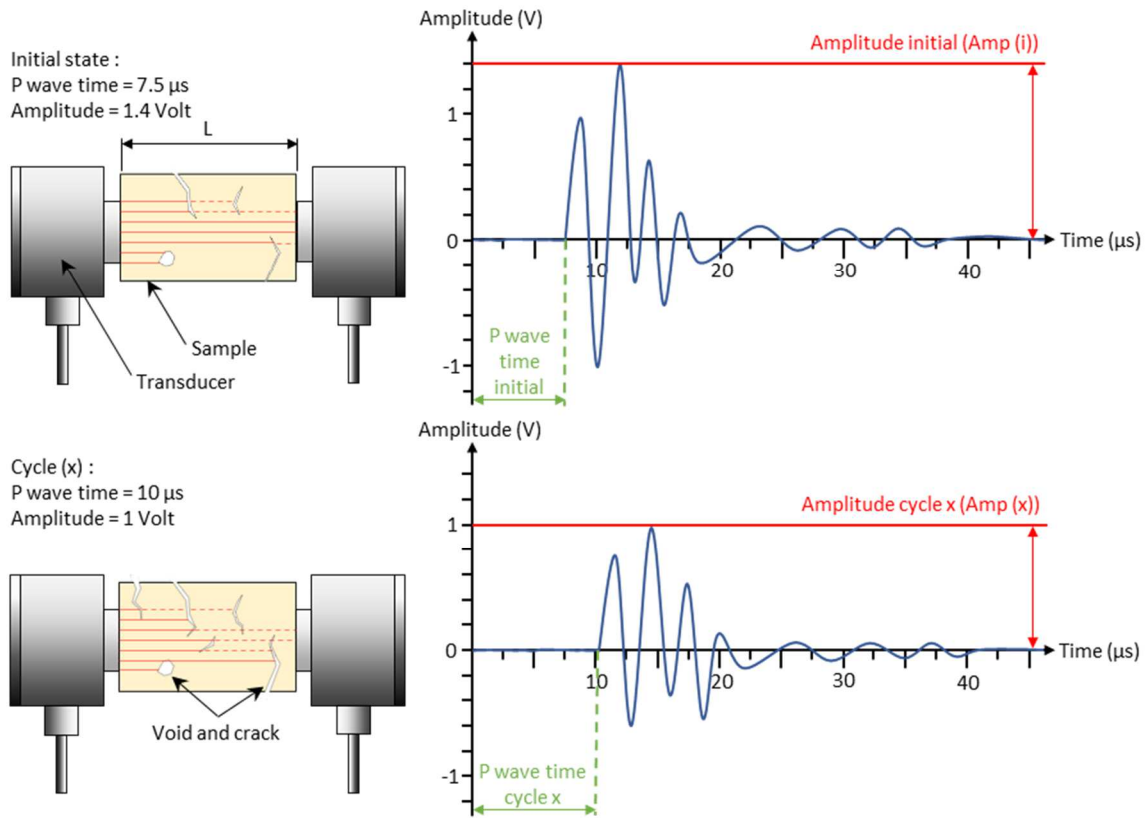
$$253 \quad E = \rho g \frac{V_p^2(1 + \nu)(1 - 2\nu)}{1 - \nu} \quad (1)$$

$$254 \quad \nu = \frac{\frac{1}{2} - \left(\frac{V_s}{V_p}\right)^2}{1 - \left(\frac{V_s}{V_p}\right)^2} \quad (2)$$

255 Where ρg is the bulk density determined through direct measurement of dried weights and
256 dimensions of samples.

257 In addition to V_p and V_s , the amplitude coefficient (A) was obtained. It was defined as the ratio
258 between the Amp (x) and the Amp (i). Amp is the maximum amplitude (in absolute values) measured
259 in the waveform of the signal received: Amp (i) corresponded to the value of the samples before the
260 tests and Amp (x) after each quenching test.

261 The quantification of this parameter allowed to estimate textural defects induced to the rock. The
262 presence of an open fracture brings about a strong scattering of the ultrasonic waves and induces a
263 decrease in coefficient A . The attenuation of the signal amplitude (Fig. 4) depends on the textural
264 characteristics of the rock and the individual defects but is less sensitive to crystal size and porosity
265 as may be V_p (Martínez-Martínez et al., 2011).



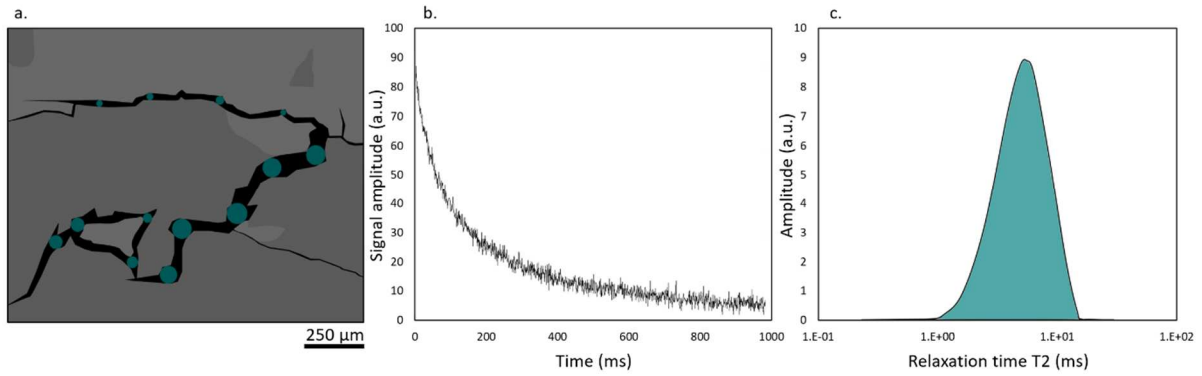
267

268 **Fig. 4: Diagram of the transmission of ultrasonic waves with an example of signals received as a**
 269 **function of the degradation of the rock.**

270 3.3.4 Nuclear Magnetic Resonance relaxometry

271 Nuclear magnetic resonance (NMR) is a fast, practical, and non-destructive tool for characterizing
 272 complex porous media. The NMR measurements were carried out on a set of 66 samples of each
 273 sound granitoid using a minispec mq-Series instrument. NMR is based on the decay by
 274 magnetisation of the hydrogen nucleus of water and useful for the deduction of certain information
 275 on the structure of pores (distribution pore) (Liu et al., 2017; Tian et al., 2020; Weng et al., 2018).
 276 The rock samples were vacuumed and saturated for 24 h and were then soaked in water for 24 h to
 277 fill the rock material with water. During the measurement, the sample was taken out from the water
 278 and instantly integrated into a hermetic support before being placed in the NMR. That maintained
 279 the saturation during the whole measurements. The NMR method estimates the diameter which
 280 corresponds to the width between the porous walls (Fig. 5).

281



282

283 **Fig. 5: Summary of the use of NMR in the analysis of porous rocks. a. Diagram of the enlarged 2D**
 284 **X-ray CT view of the SM granite to visualise the cracks, the blue circles are detected by NMR. b.**
 285 **The transverse magnetisation decay curve (example of measurement on the SM granite). c. The**
 286 **transverse relaxation time (T2) distribution curve constructed by a mathematical inversion process**
 287 **(the curve reflects a distribution of pore, surface to volume ratios V/S).**

288 The transverse relaxation time (T2) is measured with a Carr-Purcell-Meiboom-Gill (CPMG) sequence,
 289 at regular time intervals 2τ (or TE) of $100 \mu\text{s}$. The transverse magnetisation decay curve (Fig. 5b) is
 290 the sum of all decay signals generated by the protons in the sample. Dynamics Center software
 291 (Version: 2.5.5) was used to represent the distribution of relaxation times (the amplitudes A_i as a
 292 function of $T2_i$) obtained through a mathematical transformation (Laplace inverse) (Fig. 5c).

293 These are the surface effects and the physical properties that are used in nuclear magnetic
 294 relaxation in porous media. Each T2 is linked to the porous space of the sample, in particular the
 295 ratio/surface.

296 This link is transcribed in the equation (3) (Fleury, 1998), as follows:

297
$$\frac{1}{T2} = \frac{1}{T2b} + \rho \frac{S}{V} + \frac{1}{12} (TE\gamma G)^2 D \quad (3)$$

298 Where T2 represents the transverse relaxation time, ρ is the specific surface relaxivity (of the order
 299 of $1\text{-}30 \mu\text{m}\cdot\text{s}^{-1}$ for natural porous media). T2b represents the relaxation time of the fluid saturating
 300 the porous space (2700 ms for water at $30 \text{ }^\circ\text{C}$), S is the surface and V the volume of the pore
 301 considered, TE is the inter-echo time of the CPMG sequence; we set it at $100 \mu\text{s}$, G is the average
 302 local magnetic field gradient, γ is the gyromagnetic ratio and D is the auto-diffusion coefficient of the
 303 fluid. The term diffusion can be neglected in equation (3) because T2 is independent of the inter-
 304 echo time (very weak in this experiment).

305 The geometry of our pores must be hypothesised. In the monophasic case, the spherical pores have
 306 a surface ratio of:

307
$$\frac{S}{V} = \frac{3}{r} \quad (4)$$

308 where r is the pore radius. If we consider that our pores are spherical, we simplified equation (5), as
 309 follows:

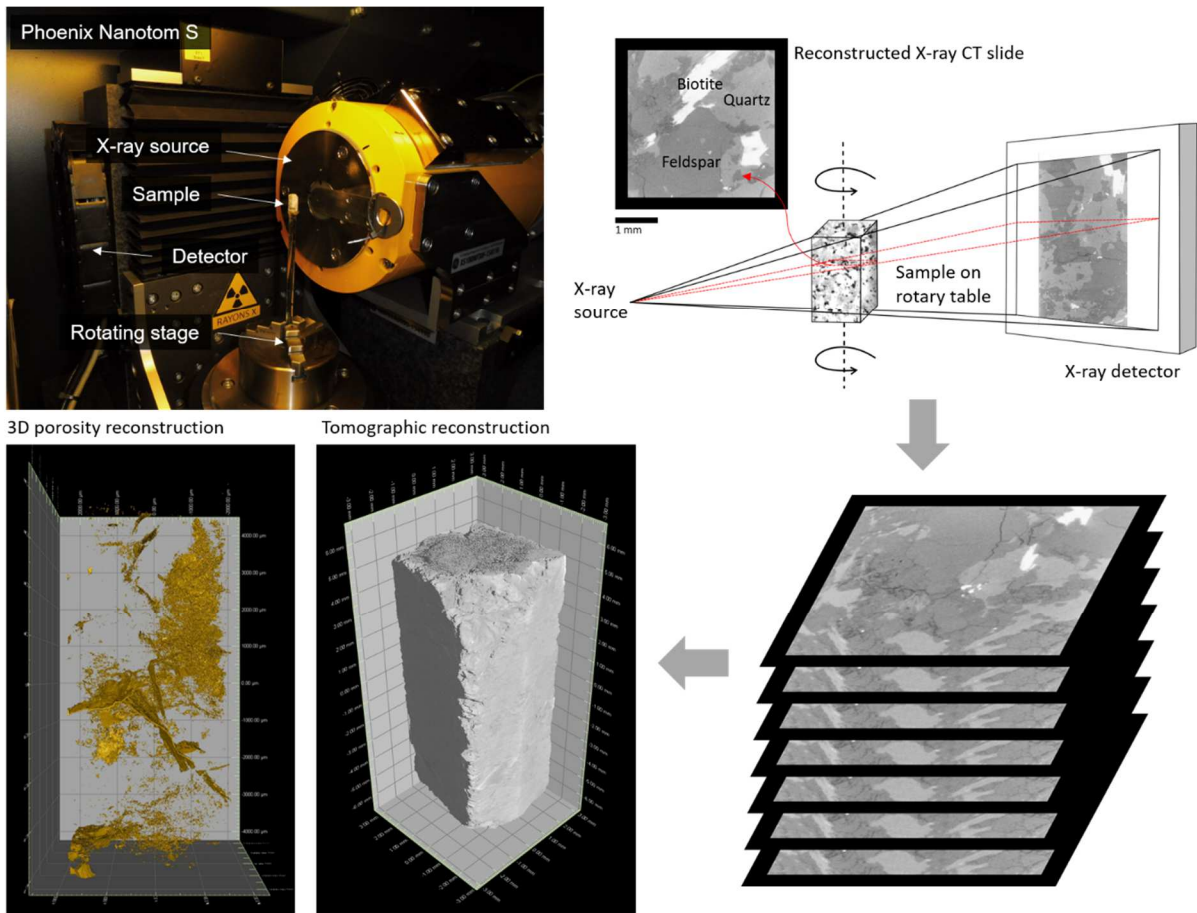
310
$$\frac{1}{T2} = \frac{1}{T2b} + \rho \frac{3}{r} \quad (5)$$

311 The values of T2 were taken before and after cycling. Thus, the T2 distribution reflects the
312 information on the pore size, the smaller the T2 value, the smaller the pore size.

313 3.3.5. X-ray micro-tomography

314 X-ray microtomography (X-ray CT) is a non-destructive technique that permits to visualise in 3
315 dimension the modifications of the porous network at high resolution, without sample preparation
316 or chemical fixation. As a result, the natural characteristics of the mineralogical information and the
317 porous network have been maintained. X-ray tomography imaging was performed on a Phoenix
318 Nanotom S. A rectangular prisms of size 5 x 5 x 10 mm of the GA and SM granite were analyzed
319 before and after 35 quench cycles. The X-ray tomography scan resolution was associated with the
320 sample size. The resolution was about 1 voxel = 6 μm. The maximum voltage that this
321 microtomograph can supply is 180KV/15W. An X-ray source generates beams which pass through
322 the sample placed on a 360 ° rotating stage, leaving shadow projections on the detector and
323 acquiring several 2D X-ray absorption images (Fig. 6). The measurement of the X-ray attenuation is
324 proportional to the local bulk density of the object if the chemical composition of the object is
325 uniform. Density values are represented by grey levels, black is equivalent to air while white is set to
326 the highest mineral density. In general, feldspar, quartz, and biotite minerals have average densities
327 of 2560 kg·m³, 2648 kg·m³ and 3090 kg·m³, respectively. Therefore, biotite will appear in light colour
328 on images scanned by X-ray tomography, and quartz and feldspar minerals will have darker colours.
329 The small difference in density between quartz and feldspar makes their identifications more
330 difficult. The sectional images of the object are reconstructed and allow to create a full 3D
331 representation of the samples. In geoscience, this technique has been widely implemented in studies
332 (Fan et al., 2018; Géraud et al., 1999; Isaka et al., 2019; Kumari et al., 2018; Sepúlveda et al., 2020;
333 Yun et al., 2013).

334



335
 336 **Fig. 6: Principle of X-ray microtomography going from image reconstruction to 3D visualisation.**

337 At the end of the acquisition process, the VGStudio MAX 2.2 © software (Volume Graphics) was used
 338 to perform the reconstruction and its qualitative and quantitative analysis. First, the volume defects
 339 associated with the acquisition were eliminated. Regions of Interest (ROI) were created respecting
 340 the capacity of the computer used and being the most representative of the entire sample. The
 341 same ROI was selected on the samples before and after treatment. The segmentation of the images
 342 allowed to separate the mineral phase from the crack porosity by attributing to each voxel of the
 343 image the corresponding phase according to its shade of grey. The porosity values of the slides were
 344 strongly influenced by the choice of the binarisation threshold. For this reason, the adjustment
 345 parameters remained the same throughout all the analysis. Different properties of the voxels
 346 (volume, diameter, sphericity, etc.) were obtained using a flaw detection tool.

347 The heterogeneity of the distribution of microcracks along the z height was evaluated. From the
 348 porosity of the X-ray CT images of the cross-sections in x – y planes, the coefficient of variation (CV)
 349 was calculated before and after the quenching. It is defined as the ratio of the standard deviation to
 350 the mean of the porosities of the sections in the xy plane.

351 3.4. Chemical analysis

352 3.4.1. X-Ray Fluorescence and Inductively coupled plasma mass spectrometry analysis

353 The chemical analysis of the granites was performed using X-Ray Fluorescence (XRF) (Philips Magix
354 Pro device), which provided information of major and trace elements.

355 The geochemical reactivity of the water-granite interaction was carried out by analysing the
356 resulting/lixivated water after one hour of water-quenching for each granite type and test every 5
357 cycles (Fig. 3b). The contents of dissolved Al, Ca, Fe, Mg, Mn, Na, K, and Ti were determined using
358 Inductively coupled plasma mass spectrometry (ICP) (VG PQ-ExCell, Thermo Elemental). Nitric acid
359 (HNO_3) was added before analysis to stabilise the solutions.

360 4. Results

361 The results of the initial physical properties of the selected stone are shown in Table 2.

362

363 **Tab. 2: Values of physical properties. ϕ_c : connected porosity C: capillary coefficient; Vp: P-wave**
364 **propagation velocity; Amp: maximum amplitude of the P-waves; Vs: S-wave propagation velocity;**
365 **E: Young's modulus and T2: transverse relaxation time.**

Stone	ϕ_c (%)		C ($\text{g}\cdot\text{m}^{-2}\cdot\text{s}^{-1/2}$)		Vp ($\text{m}\cdot\text{s}^{-1}$)		Amp (V)		Vs ($\text{m}\cdot\text{s}^{-1}$)		E (GPa)		T2 (ms)	
	Avg.	St.d.	Avg.	St.d.	Avg.	St.d.	Avg.	St.d.	Avg.	St.d.	Avg.	St.d.	Avg.	St.d.
A	5.20	0.48	13.26	2.54	2526	322	5.6×10^{-04}	2.9×10^{-04}	1066	147	7.93	1.99	10.7	2.0
GA	1.19	0.35	2.39	0.45	3292	118	8.0×10^{-03}	4.1×10^{-03}	1549	94	17.22	2.07	38.8	4.0
GS	3.75	0.64	14.23	1.00	1758	197	1.0×10^{-03}	4.8×10^{-04}	889	149	5.30	1.69	25.0	2.8
SM	2.40	0.30	8.92	3.25	3951	308	4.1×10^{-03}	1.7×10^{-03}	1657	260	20.24	6.42	11.7	2.1

366 Avg average, St.d standard deviation

367

368 The degree of initial weathering of the four granites was assigned relative to their initial porosity.

369 Albero (A) will be referred to as a highly weathered granite with the highest porosity of 5.2%.

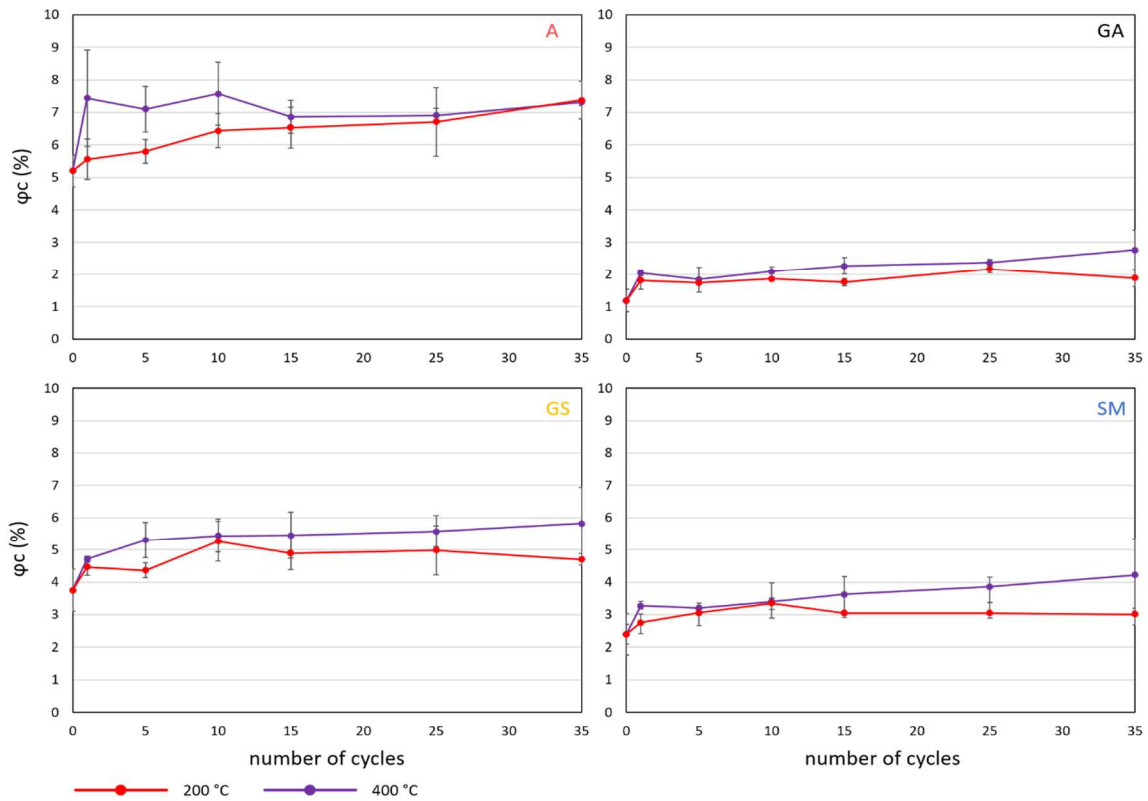
370 Therefore, it showed low Vp and Vs values of about 2526 and 1066 $\text{m}\cdot\text{s}^{-1}$, respectively. Gris Alba (GA)
371 will be referred to as an unaltered granite with a low porosity of 1.2%. This granite showed the
372 lowest values of the maximum amplitude of Vp. It showed the highest relaxation time T2 values.

373 Golden Ski (GS) will be referred to as a moderately weathered granite with a porosity of 3.75%. It
374 showed a highest C coefficient and lowest value of Vp and Vs of approximately 1758 and 889 $\text{m}\cdot\text{s}^{-1}$,
375 respectively, resulting in a low value of the elastic modulus E of 5.3 GPa. Silvestre Moreno (SM) will

376 be referred to as a slightly weathered granite. It showed a porosity of around 2.4% and the highest
 377 V_p , V_s and E values.

378 4.1. Connected porosity

379 The water porosity was calculated before the test and on the samples removed during the cycles
 380 (Fig. 7).



381
 382 **Fig. 7: Relationship between the number of thermal cycles and the connected porosity (ϕ_c) for the**
 383 **two quenching tests at 200 °C and 400 °C.**

384 For each granite, the porosity showed an increasing trend with the quenching cycles, more
 385 remarkable after the first cycle, and greater when heated at 400 °C than at 200 °C. This increase was
 386 not monotonous for all granites. Indeed, ϕ_c decreased slightly for A from the first to the fifth cycle at
 387 400 °C for example.

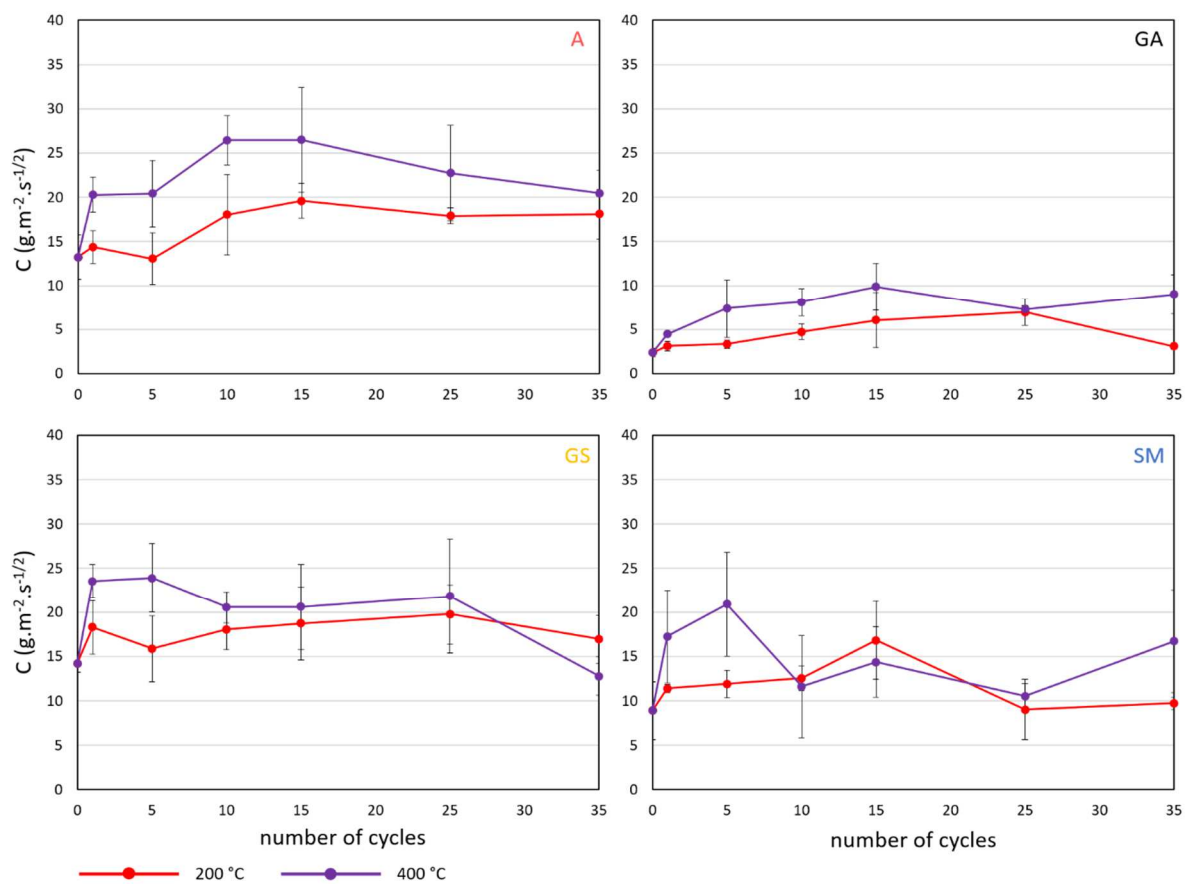
388 For A, the cycles at 200 °C revealed that the ϕ_c increased continuously with the number of cycles,
 389 with a change of 40% at the end of the test. At 400 °C, the ϕ_c did not show any further increase after
 390 the first cycle, with an abrupt increase of also around 40%.

391 For GA, at 200 °C the ϕ_c increased after cycle 1 and 25, with a variation of 60% at the end of the test.
 392 At 400 °C, after an abrupt increase during the first cycle, ϕ_c grew continuously until the end of the
 393 test with a change of 130%.

394 For GS and SM, the curves of the cycles at 200 °C indicated 2 slopes, a first until cycle 10 with
 395 continuous increase and a second from cycle 10 to 35, which showed a stabilisation, with a final
 396 variation of 25% at the end of the test. The curves at 400 °C of these 2 granites showed as for the
 397 rest of the rocks, an abrupt increase after the first cycle and a softer augmentation through the
 398 cycles, with a final increase of 55 and 75% for GS and SM respectively.

399 4.2. Capillary coefficient

400 The capillary absorption curves lasted over 72 hours, where the capillary coefficient (C) was obtained
 401 after the first linear part of the curve. The rise of the capillary fringe was complete for A, GS, and SM.
 402 For the GA granite, the water weight gain curve showed several breaks in slope and the capillary
 403 fringe did not reach the top of the sample. This incomplete rise reflected the low porosity values as
 404 well as the poor interconnection between the multiple families of pores and cracks. Figure 8
 405 represents the evolution of the coefficient C of each granite during the two quenching tests.



406
 407 **Fig. 8: Relationship between the number of thermal cycles and the capillary coefficient (C) for the**
 408 **two quenching tests at 200 °C and 400 °C.**

409

410 For both quenching tests, capillary water absorption increased from the first cycle for all granites. In
411 general, the increase was greater for rocks heated at 400 °C.
412 For A, at cycle 15, the coefficient C reached its highest value for rocks preheated at 200 °C with an
413 increase of about 50%, and at cycle 10 for rocks preheated at 400 °C with an increase of about 100%.
414 It only took one cycle of the preheated rock at 400 °C to reach a rise of 50%. From cycle 15, the
415 coefficient C decreased for the two quenching tests and ended at cycle 35 with a final increase of
416 35% for the tests at 200 °C and of 55% for the tests at 400 °C.
417 For GA, although the general increase was significant for both quenching tests, the progression was
418 greater on rocks preheated at 400 °C. The C coefficient of rocks preheated at 200 °C increased by
419 200% in a linear trend until cycle 25. This increase was comparable to the increase observed during
420 cycle 5 of rocks preheated at 400 °C. From cycle 15, the coefficient C of rocks preheated at 400 °C
421 stabilised after an increase of about 310%.
422 For GS, the capillary water absorption showed an irregular progression for the two quenching tests
423 after an abrupt increase after cycle 1. The coefficient C increased to a maximum of 40% at cycle 25
424 for the 200 °C tests and 70% at cycle 5 for the 400 °C tests.
425 For SM, the rocks preheated at 200 °C, the coefficient C increases by 80% after cycle 15. The
426 coefficient remained stable from cycle 25. Rocks preheated at 400 °C increased significantly by 130%
427 after cycle 5.

428 4.3. P- and S-waves velocities and dynamic elastic moduli

429 Figure 9 shows the variations of the average of P-waves propagation velocities (V_p) and the
430 attenuation coefficient (A) with the number of cycles. Each point corresponds to the average of the
431 18 samples measured from the initial state to cycle 35.

432 The granites preheated at 200 °C showed initially a gradual decrease in V_p with the number of
433 cycles. A, GS, and SM exhibited a later stabilisation or even a slight recovery. Granites preheated at
434 400 °C showed a significant decrease in V_p after the first cycle, *i.e.* by approximately 26%, 15%, 23%,
435 and 22% for A, GA, GS, and SM, respectively. Following this phase, the variations were smaller. The
436 average rate of V_p decreased at cycle 35 by 34%, 25%, 23%, 27% for A, GA, GS, and SM, respectively.

437

438 For A, V_p gradually decreased by about 10% until cycle 14 at 200 °C, then remains stable. The
439 coefficient A remained close to the initial value from the beginning at 200 °C. For 400 °C, V_p showed
440 an overall decreasing trend with increasing cycles. The coefficient A decreased by about 40% after
441 cycle 14 and then increased again.

442

443 For GA, Vp values did not show a significant variation, whereas coefficient A showed significant
444 variation. The first cycles were marked by an increase followed by a decrease of about 60% after
445 cycle 14 at 200 °C. The coefficient A increased again to reach the attenuation values of the initial
446 wave. For 400 °C, Vp and the coefficient A decreased linearly up to cycle 35.

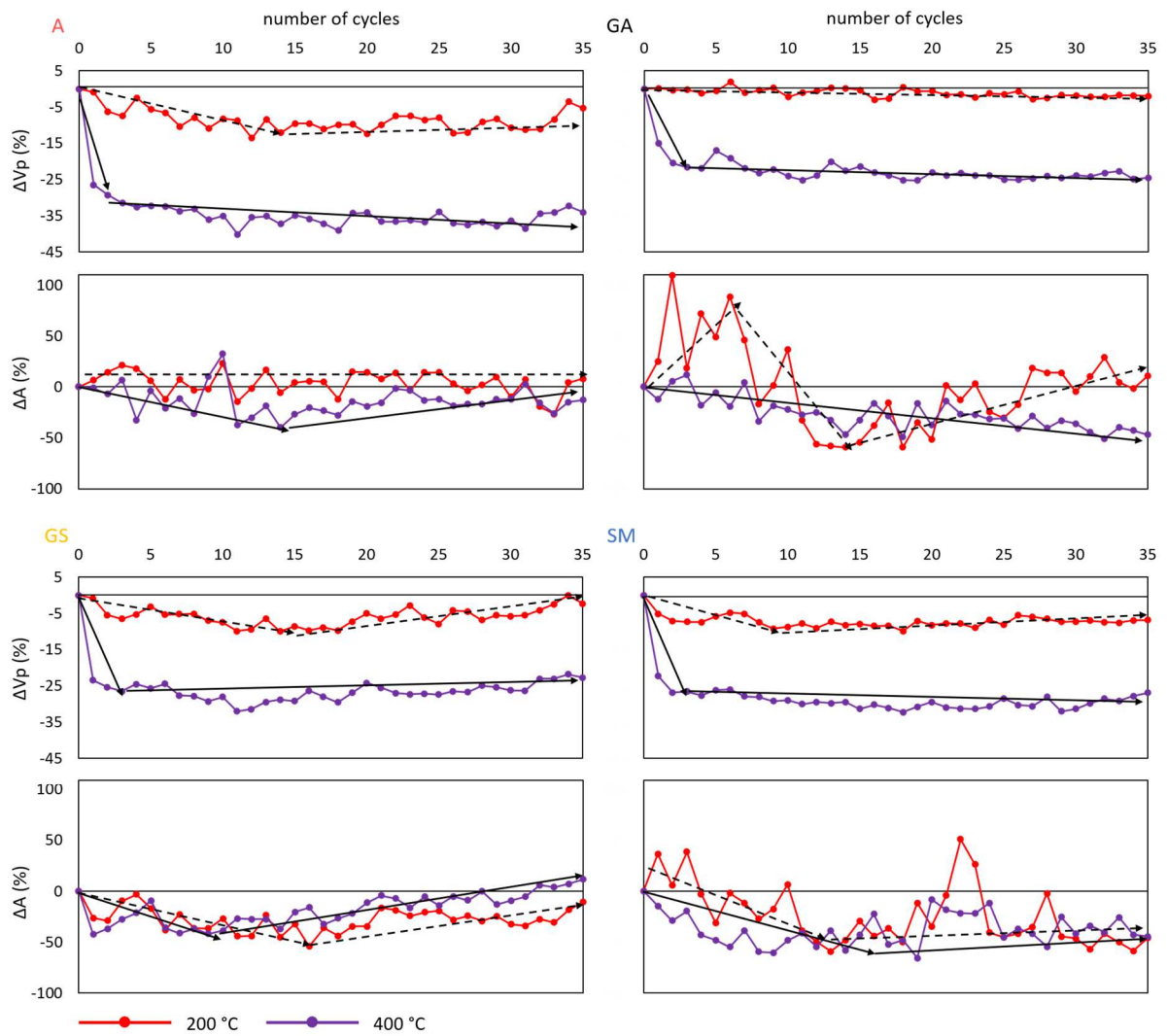
447

448 For GS, Vp decreased by approximately 10% until cycle 18 then gradually increased to reach the
449 initial mean value again at cycle 33 at 200 °C. The coefficient A showed a similar trend with a
450 decrease of approximately 50% after cycle 16, followed by an increase at 200 °C. For 400 °C, GS was
451 the only one among the granites to have these Vp values which increased after the large falling after
452 the first thermal shock cycles. The coefficient A also gradually increased after a decrease of about
453 40% after the first cycle.

454

455 For SM, a decrease of Vp of about 10% was observed after cycle 10, then a stable recovery to -7% of
456 the initial value at 200 °C. After a balancing phase during the first 10 cycles, the coefficient A
457 decreased by about 60% after cycle 13, then hovered around -40%. It is also noted that the values
458 between samples had a high variability. For 400 °C, after a decrease at the first cycle, Vp remained
459 between -20 and -30%. The coefficient A decreased by approximately 60 % at cycle 17, then
460 increased slightly.

461

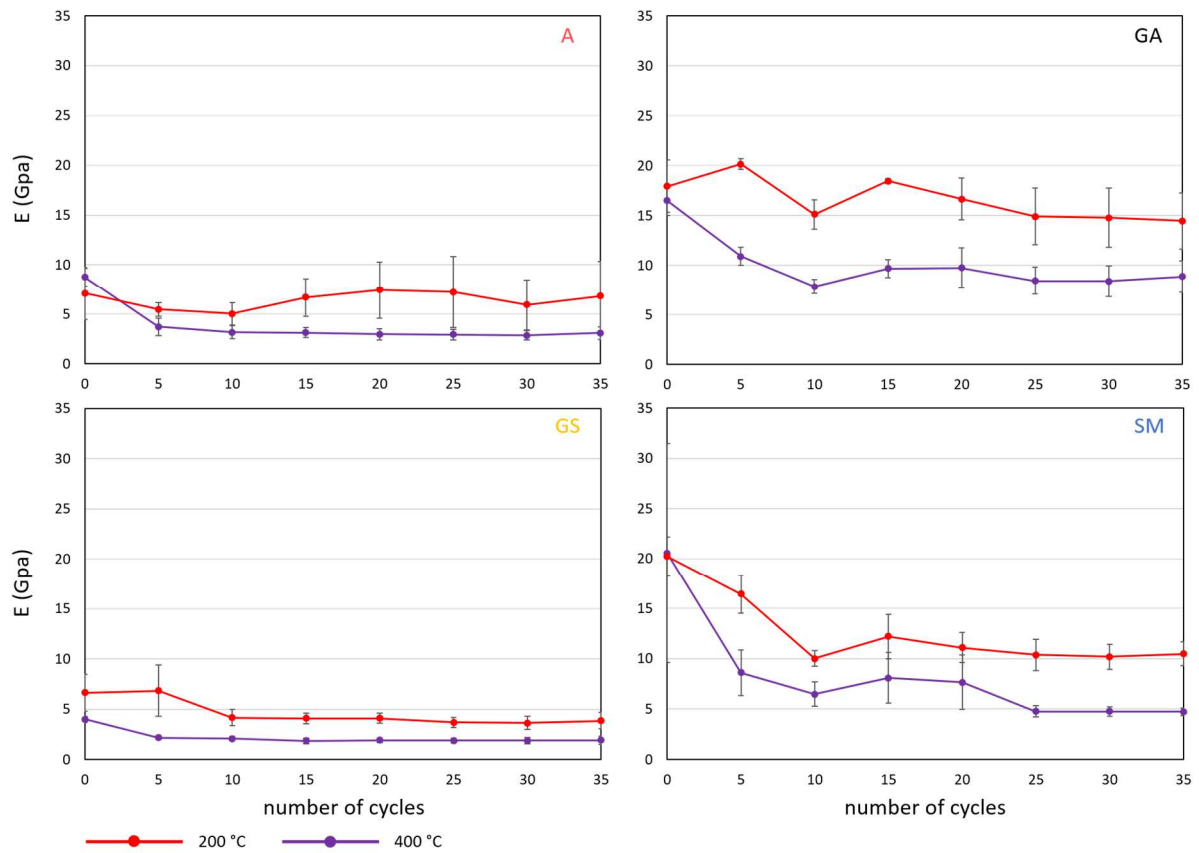


462
463
464
465

Fig. 9: Relationship between the number of thermal cycles and the percentage change in the P-waves velocity (Vp) and the amplitude coefficient (A) with the initial state. Solid and dashed black lines represent the trend for 200 °C and 400 °C, respectively.

466

467 The changes of the elastic modulus (E) of granites after heating (200 °C and 400 °C) and treatment
468 with water are shown in Figure 10.



469

470 **Fig. 10: Relationship between the number of thermal cycles and the Young's Modulus (E) for the**
471 **two quenching tests.**

472 For A, E decreased by approximately 20% from the first 5 cycles at 200 °C. Then, A remained stable
473 around its initial value. For 400 °C, the values of E decreased significantly after 5 cycles, *i.e.* by about
474 60%, and then remained stable.

475 For GA, E showed an increase of 10% at cycle 5 then a decrease of 20% after cycle 35 at 200 °C. For
476 400 °C, the values of E decreased by 35% and 45% after 5 and 35 thermal treatments, respectively.

477 For GS, E remained stable after a 40% decrease after cycle 10 at 200 °C. For 400 °C, the values of E
478 decreased by 45% and 50% at 400 °C after 5 and 35 thermal treatments, respectively.

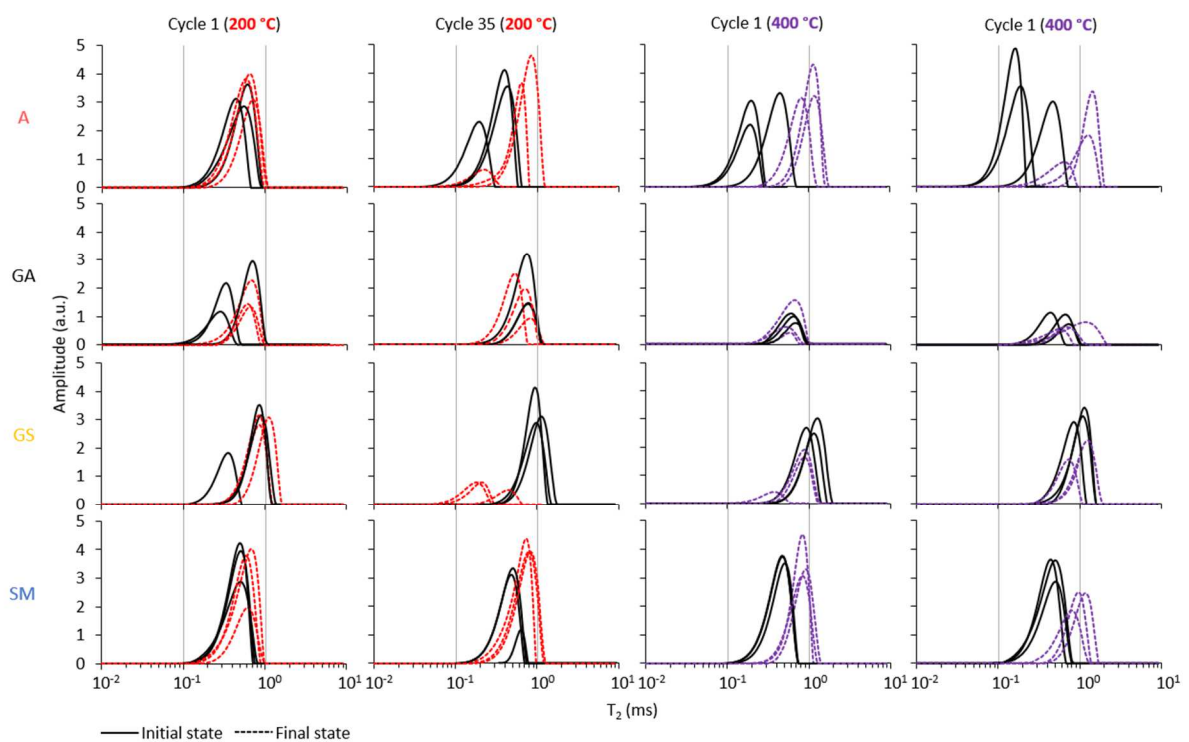
479 For SM, E decreased by approximately 20% from the first 5 cycles at 200 °C and reached a decrease
480 of 50% after cycle 35. For 400 °C, the values of E decreased by 60% and 80% at 400 °C after 5 and 35
481 thermal treatment, respectively.

482 4.4. Nuclear Magnetic Resonance relaxometry

483 We compared quantitatively the microstructure evolution of the studied granites using the
484 transverse relaxation time, T₂ (Fig. 11).

485 The quenching test at 200 °C did not show any variation during the first cycle, although at the end of
486 the test A and SM increased their T₂ values and showed a slightly greater amplitude. GA showed a
487 slight decrease and GS shifted and reduced notably its signal (tighter cracks).

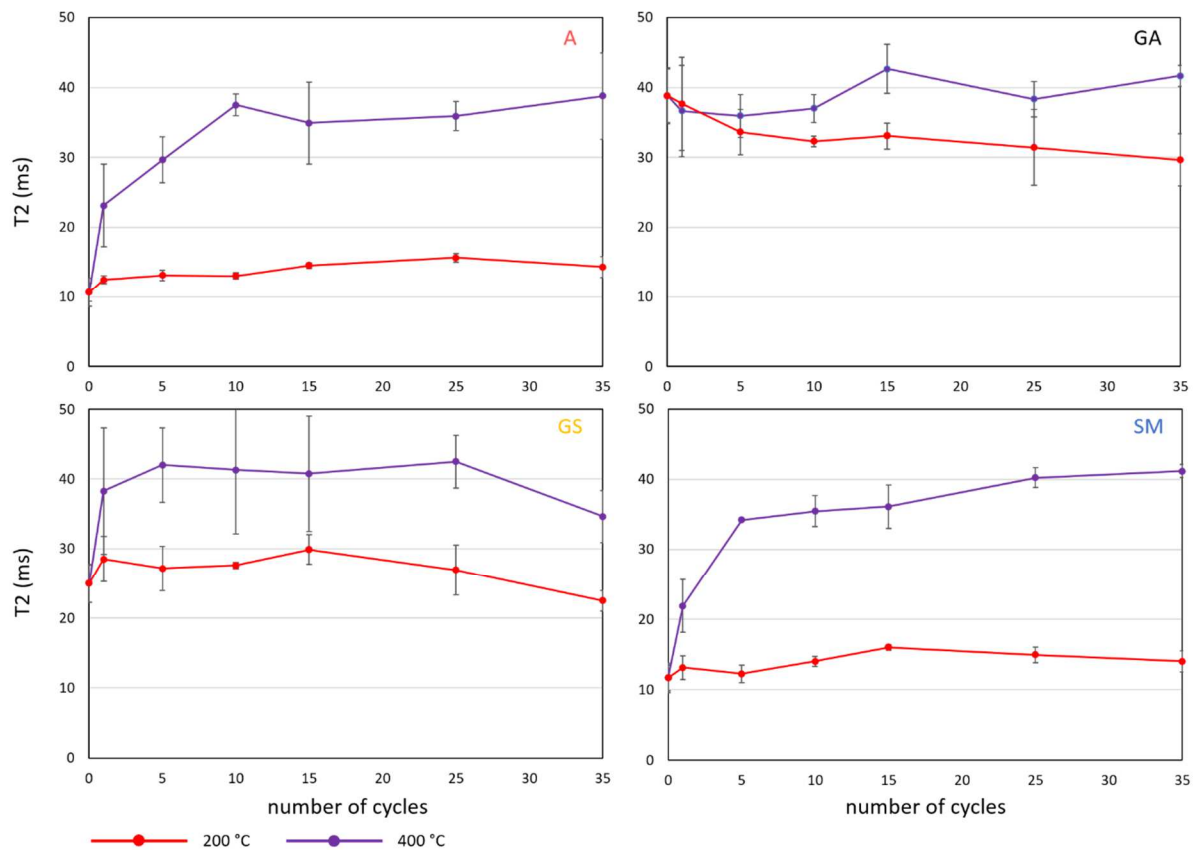
488 During the first cycle at 400 °C, A and SM evolve to similar values. GA kept a low signal amplitude
489 before and after quenching and GS slightly decreased its amplitude. At the end of the test, A and SM
490 slightly decreased their amplitudes but increased their T₂ values. GA and GS showed little change
491 from their initial state.



492

493 **Fig. 11: Evolution of the transverse relaxation time (T₂) distribution curves after 1 and 35 cycles.**
494 **The initial and final state corresponding to the same samples.**

495 In summary, A and SM showed similar behaviour to quenching with a slight increasing evolution of
 496 the geometric mean of this T2 distribution at 200 °C and a significant evolution from the first's cycles
 497 at 400 °C (Fig. 12). The general trend of GA does not show a clear change, and a slight decrease was
 498 still noted during cycles at 200 °C. Quenching at 200 °C on GS showed little change until cycle 15 and
 499 then decreased. Cycles at 400 °C showed an increasing phase up to cycle 5, and after stabilisation up
 500 to cycle 25, T2 values decreased.



501

502 **Fig. 12: Relationship between the number of thermal cycles and the transverse relaxation time**
 503 **(T2) for the two quenching tests.**

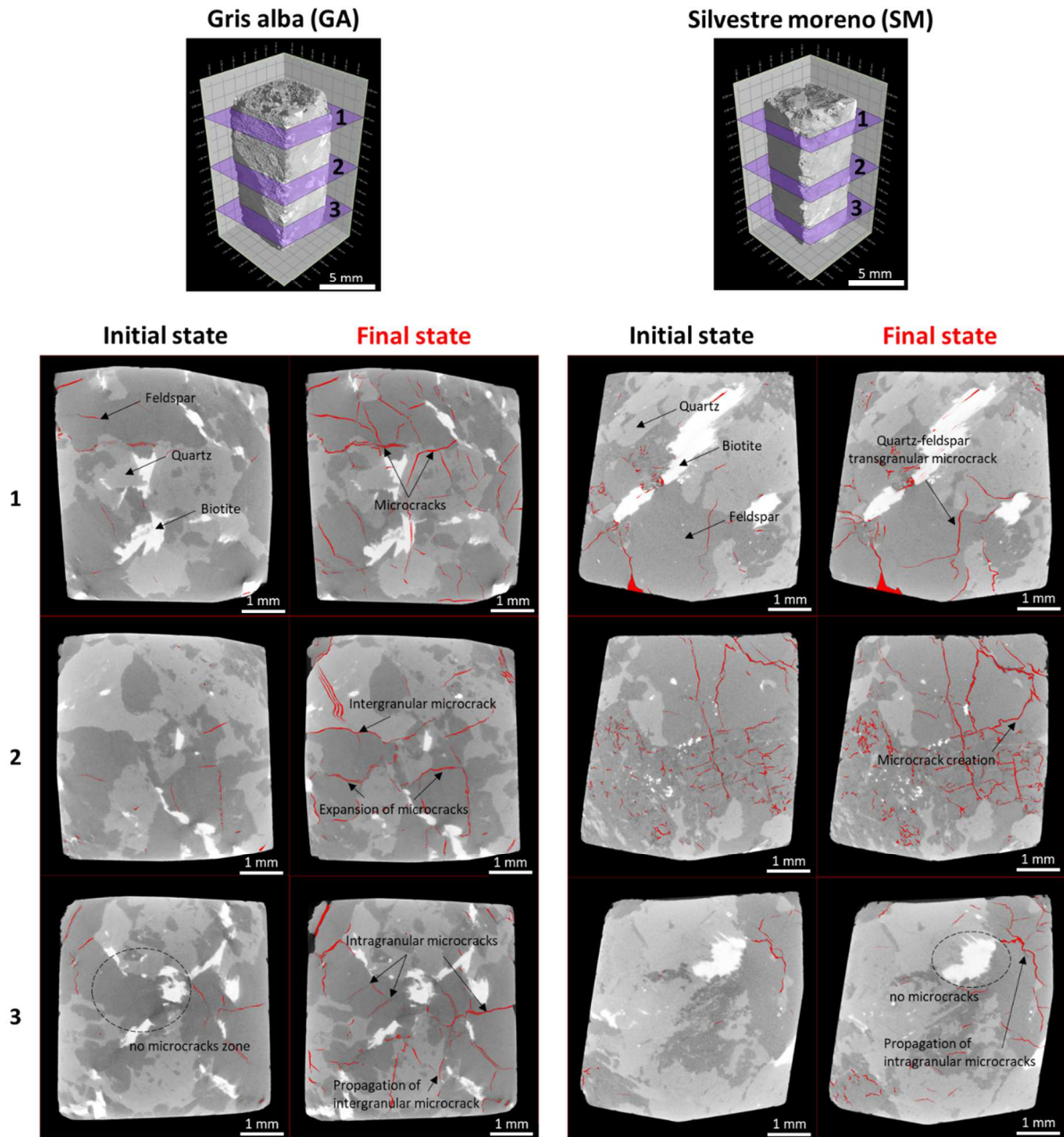
504 4.5. Microstructural analysis with X-ray CT

505 GA and SM were assessed before and after 35 quenching cycles at 400 °C because their thermal
 506 sensitivity (Vazquez et al., 2018) and also since their porosity and Vp values come closest to granites
 507 widely studied and subjected to high temperature treatments (Vp greater than 3000 m.s⁻¹ and a low
 508 porosity of close to 1% (W. Zhang et al., 2018). To establish the microcrack distribution of the studied
 509 rocks, three X-ray CT images of cross-sections in the x - y planes along the z height were taken before
 510 and after the test at 400°C, and they are shown in Figure 13. They exhibited significant microcracking
 511 at a resolution of 6 μm.

512 For GA, the initial state revealed mainly intra and intergranular microcracks in feldspars that
 513 sometimes are prolonged to quartz. After quenching cycles, the development of intergranular

514 microcracks along the quartz-feldspar crystal boundaries were detected. Some of these cracks
515 extended and formed intragranular cracks mainly in feldspars although also visible in quartz. As
516 observed by Isaka et al. (2019), microcracks in granites preheated up at 400 °C seem to stop their
517 progression when they encounter a crystal of biotite since the energy follow the path of the mica
518 boundary. Indeed, very few microcracks were observed inside the biotite. Some showed their
519 cleavage to open up after treatment (Fig. 13).

520 For SM, the fresh rock revealed that the initial microcracking was more notable than in GA granite,
521 with mainly long intragranular cracks that can be transformed into transgranular always through
522 feldspars, and also a network of and short cracks as a result of feldspar alteration. After quenching
523 test, the most remarkable change was the widening of pre-existent microcracks that prolonged as
524 intragranular microcracks and that predominated over the creation of new ones. The mica was not
525 attained by severe microcracking since the energy was absorbed and dissipated by their grain
526 boundaries as in GA.



527

528 **Fig. 13: Horizontal X-ray CT slides of GA and SM initial and final state (cycle 35) for three different**
 529 **elevations. The pores and cracks are presented in red color.**

530

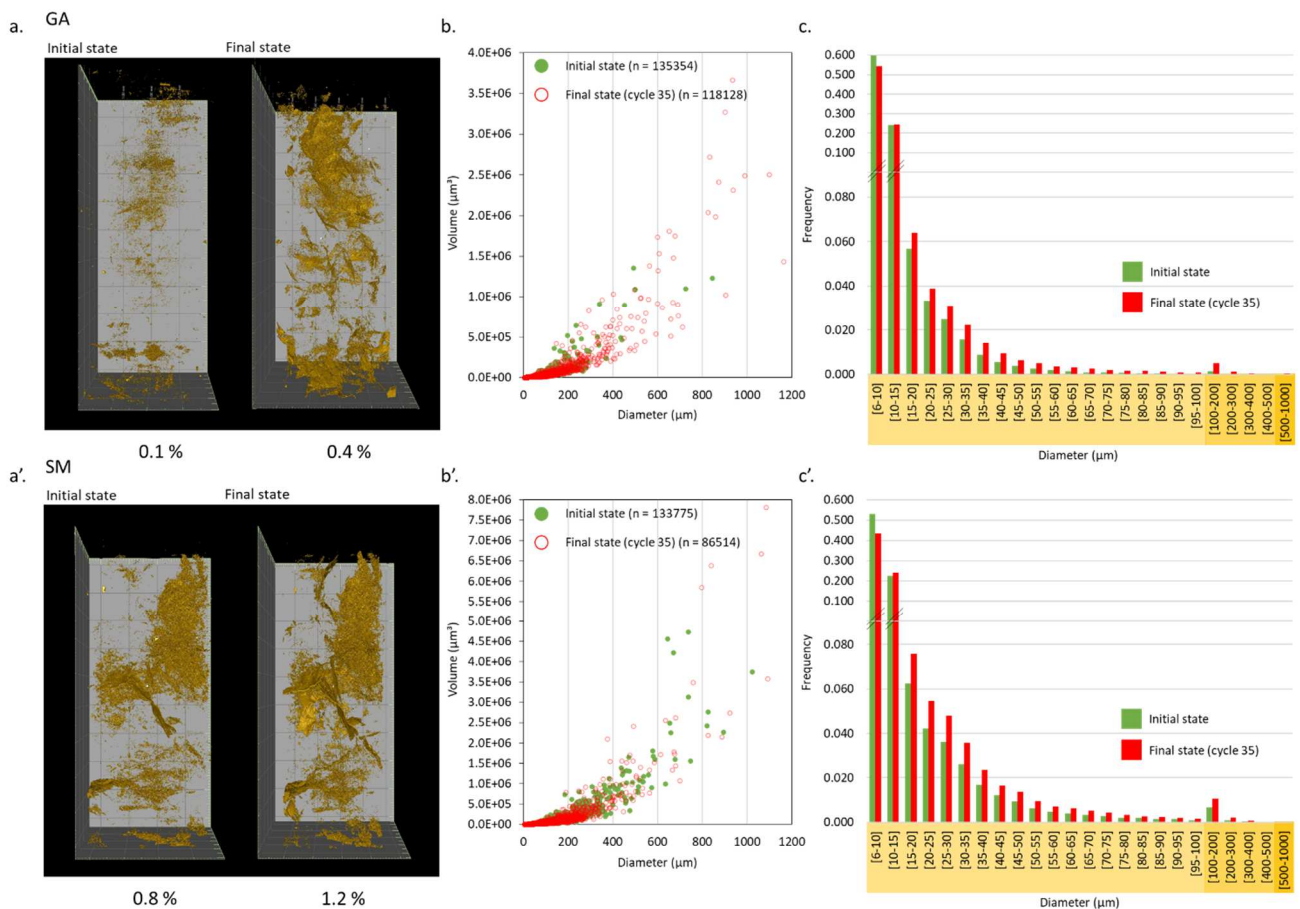
531 From the volume analyse of the X-ray CT data, a quantification of the microcrack variation can be
 532 obtained (Fig. 14). In general, the volume rendering of the porous networks showed that
 533 microcracks development were distributed evenly throughout the sample, before and after the tests
 534 so that the whole sample was affected by the quenching process. The porosity after treatment was
 535 3.5 times greater for GA and 1.5 times for SM. The evolution in the degree of microcracking in the
 536 two granites increased the coefficient of variation (CV). At the initial state, this coefficient CV was

537 80% for both GA and SM and it increased to 85% and 108%, respectively after 35 quenching cycles at
 538 400 °C.

539 In detail, image processing allowed the cracks to be detected and segmented. The parameters of the
 540 porous network (pore volume, pore number and diameter) were quantified and they are shown in
 541 Figure 14.

542 For GA, a notable increase (325%) of the pore volume was observed after quenching from 1121 to
 543 4766 μm^3 meanwhile the number of pores decreased by 13%. The quantification of the pore volume
 544 as a function of their diameter, represented in Figure 14b, showed the formation of large pores
 545 (greater than 800 μm) during the final state of quenching. The histogram (Fig. 14c) showed the pore
 546 size distribution of GA before and after quenching. The frequency of pores increased for all pore
 547 class except the smallest between 6-10 μm .

548 SM showed a smaller increase in pore volume (133%), with an average volume rising from 7175 to
 549 16736 μm^3 . However, the number of pores was reduced more significantly with a value of 35% (Fig.
 550 14 b'). The histogram (Fig. 14c') evidence that pore diameters ranging from 6 to 15 μm predominate
 551 in the sample. After heat treatment, the number of pores or cracks with a diameter greater than 10
 552 μm increased.



553

554

555 **Fig. 14: Qualitative and quantitative data extracted from X-ray CT measurements before and after**
556 **the quenching test (cycle 35). a-a'. Reconstruction of the 3D porous network. b-b'. Relationship**
557 **between volume and diameter of pores. c-c'. Pore size-frequency distribution.**

558 4.6. Mineral composition determined using XRF and chemical analysis of fluids

559 The granites in this study were mainly composed of quartz, K-feldspar, plagioclase, and micas. Table
560 3 shows the initial chemical composition of the granite samples determined by XRF, with slight
561 variations between them.

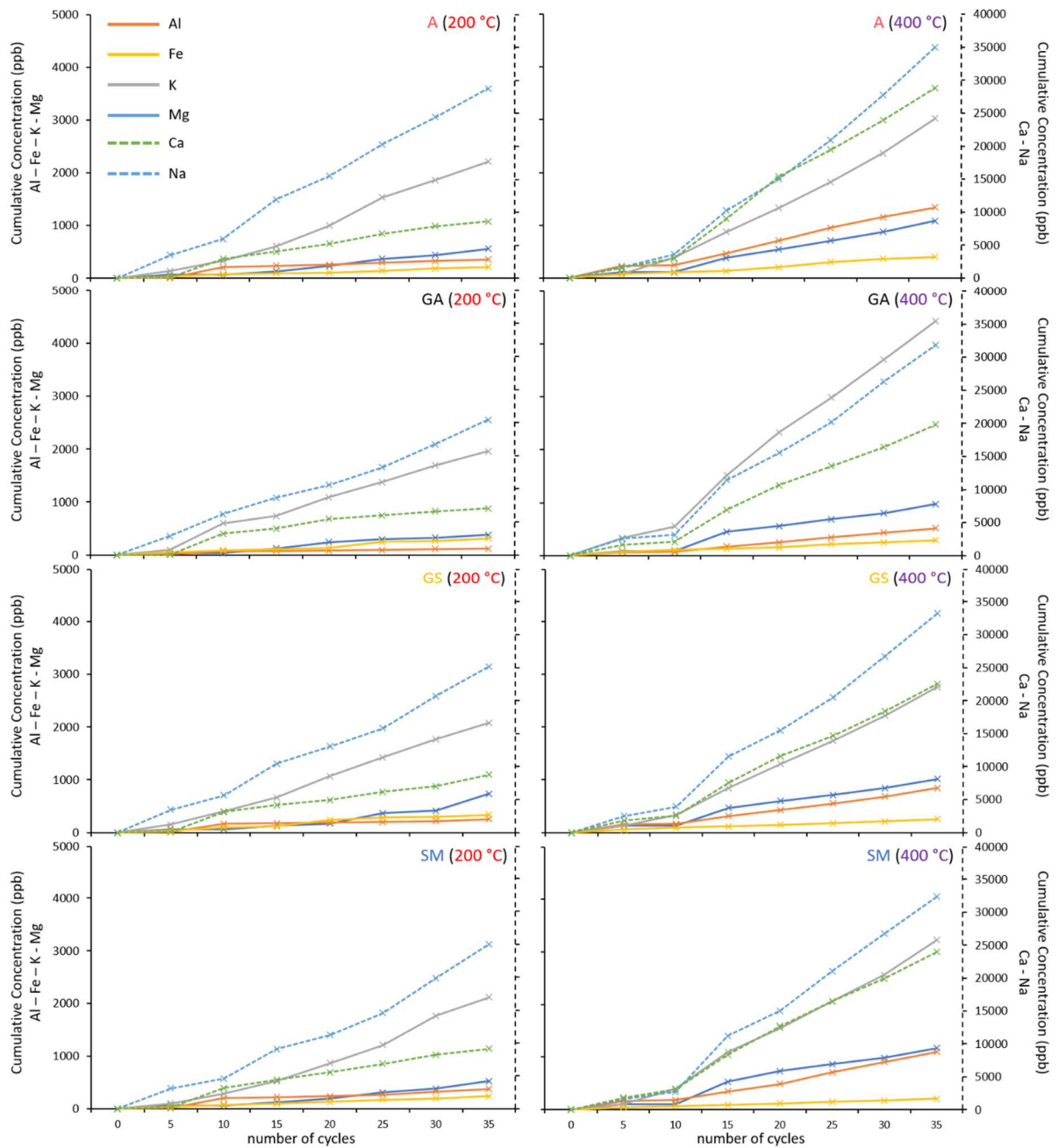
562

563 **Tab. 3: Chemical composition of the major elements expressed in percent.**

	Na ₂ O	MgO	Al ₂ O ₃	SiO ₂	K ₂ O	CaO	Fe ₂ O ₃
A	2.50	0.50	13.85	74.09	4.97	1.12	1.26
GA	3.42	0.70	14.38	71.26	5.52	1.54	1.58
GS	2.99	0.34	13.88	74.26	5.21	0.79	1.49
SM	3.29	0.46	14.43	73.35	5.92	0.52	1.42

564

565 Mineralogical and chemical alteration processes were carried out thanks to the ability of water to
566 access the rock matrix via micro-fractures (Wogelius et al., 2020). This process then allows to
567 mobilise part of the natural radionuclides and other trace elements from the primary minerals of the
568 rock matrix as they are degraded. Figure 15 showed the cumulative concentration of dissolved
569 elements as a function of the cycles on the water used for cooling.



570

571 **Fig. 15: Cumulative curves of the concentration (ppb) in Al, Fe, K, Mg, Ca, and Na in the solutions**
 572 **as a function of the number of cycles for the two quenching tests.**

573 ICP-MS analysis showed an increase in the release of minerals in the liquid phase during cycles, more
 574 intense at 400 °C. In cycles at 200 °C, all the elements were dissolved with an almost linear trend.

575 Tests at 400 °C showed an inflexion point after 10 cycles, from which the dissolution rate became
 576 faster and at the end of the experiment (cycle 35) the dissolution was greater than for the 200 °C
 577 tests.

578 5. Discussion

579 Figure 16 relates the four main parameters (initial porosity φ_c , capillary coefficient C , maximum
580 signal amplitude of ultrasonic waves Amp , P-wave velocity V_p and Young's modulus E) used to judge
581 the initial alteration of the granites in this study. The main observations are described below:

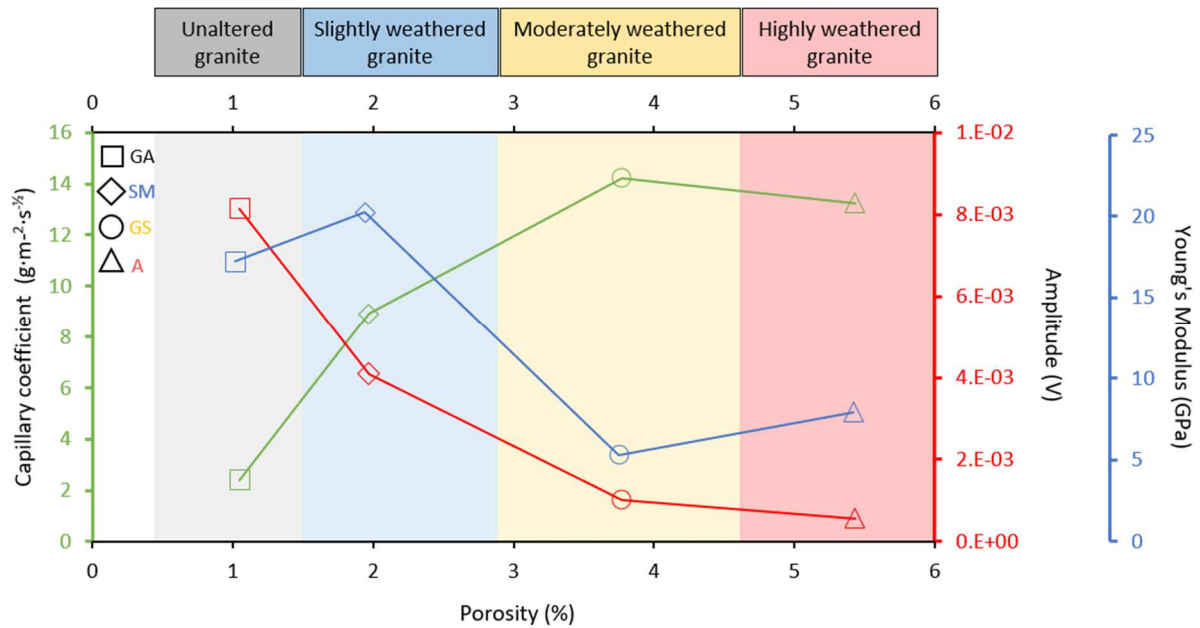
582 The unaltered granite (Gris Alba, GA) had the greatest value of ultrasonic wave amplitude, which
583 resulted in a weakly attenuated ultrasonic signal compared to A, GS, and SM. Among all the granites,
584 the unaltered granite exhibited the highest T2 values. This result was not apparently consistent with
585 the porosity values, but the relaxation rate can be increased depending on the concentration and
586 the mineralogical form of iron oxides for example (Keating and Knight, 2006) and the clay content
587 can also reduce the pore size of weathered granite.

588 The slightly weathered granite (Silvestre Moreno, SM) had the highest Young's modulus values,
589 which indicated high rigidity and a low amount of damage within the structure.

590 The moderately weathered granite (Golden Ski, GS) had the lowest mechanical properties and the
591 highest capillary coefficient values. The capillary absorption coefficient was directly linked to the
592 pore size and quantified the flow mechanisms influenced by the pore structure and the
593 interconnectivity of the pores (Benavente et al., 2002; Cai and Yu, 2011; Çelik and Kaçmaz, 2016).

594 The moderately weathered granite, the transverse relaxation time T2 values in NMR were the
595 highest among the initially weathered granites, indicating a large pore size allowing good migration
596 of the fluid.

597 The highly weathered granite (Albero, A) presented the largest pore volume. The ultrasonic wave
598 attenuation of this granite was the highest, due to the individual microcracks distributed in the
599 sample (Benavente et al., 2020). The low V_p values in the moderately and highly weathered granite
600 were indicative of the high initial microcrack density.



601

602 **Fig. 16: Relationship between the initial porosity of the granites and their capillary coefficient,**
 603 **maximum amplitude of the P-waves, and Young modulus.**

604 5.1. Effects of repeated quenching on damage

605 In geothermal engineering, extracting heat from deep rocks by injecting water into the well brings
 606 about a quenching process. The repetition of this operation can induce instability in the drilling at
 607 the expense of its profitability. The degree of cracking depends mainly on temperature and pressure
 608 stress, mineralogical composition, and particle size distribution (Freire-Lista et al., 2016). Due to this
 609 brutal thermal gradient during quenching, a thermal expansion occurs in the structure resulting in a
 610 thermal shock cracking (Kumari et al., 2018).

611 Quenching generally leads to tensile stress tangential to the surface of the rock. After a thermal
 612 shock, the damage near the surface is often greater than inside the sample (Fan et al., 2020). The
 613 damage to the surface of the granite sample may become more concentrated, resulting in
 614 nucleation of surface microcracks (Yu et al., 2020). The theoretical relationship exposed by Kim et al.
 615 (2014) allows estimating the maximum tangential tensile stress generated at the surface of the
 616 granites studied (σ_t max) (Tab. 4).

617
$$\sigma_t = \frac{E\alpha \Delta T}{1-\nu} \quad (6)$$

618 where E is the average Young's modulus of samples fast cooled from 200 or 400 °C respectively, α is
 619 the thermal expansion coefficient, ΔT is the difference temperature, and ν is the Poisson's ratio. The
 620 calculations for the studied granites used the thermal expansion coefficients from Vazquez et al.
 621 (2011, 2015).

622 **Tab. 4: Maximum tangential tensile stress generated (σ_t max) at the surface of the granites during**
 623 **the quenching after the two preheating treatments and experimental tensile strength test**
 624 **(Vazquez et al., 2018¹).**

625

	Mechanical properties: Tensile strength (MPa) ¹	σ_t max (MPa)	
	25 °C	200 °C	400 °C
Unaltered granite (GA)	9.3	41.9	50.5
Slightly weathered granite (SM)	4.9	43.3	48.9
Moderately weathered granite (GS)	4.0	15.8	12.2
Highly weathered granite (A)	4.4	16.3	22.1

626

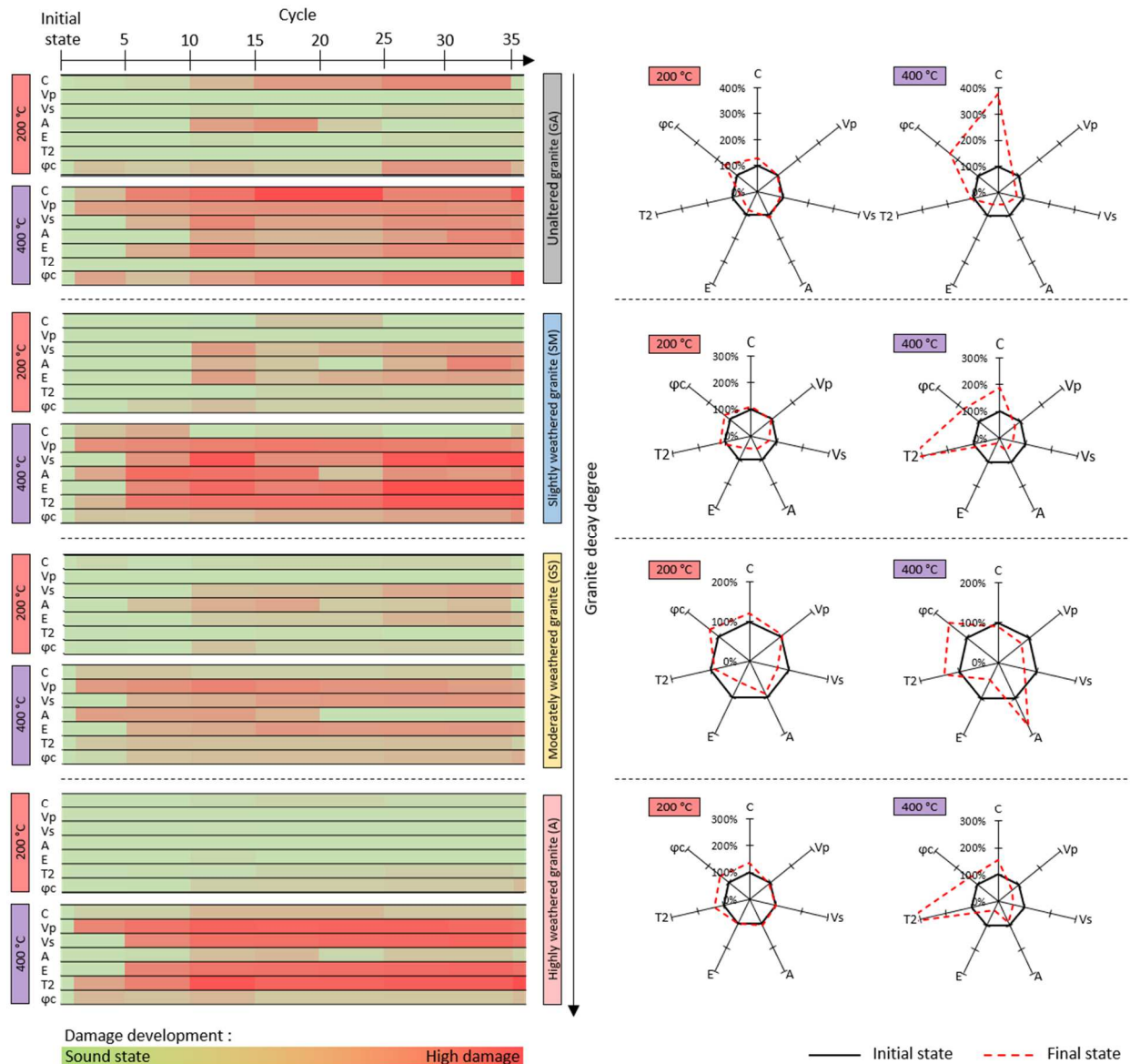
627 The maximum tensile stresses that could be generated at the rock surface during quenching are
 628 much greater than the tensile strength of these granites measured experimentally at room
 629 temperature (Tab. 4, Vazquez et al., 2018). Samples preheated at 400 °C and then immersed in cold
 630 water (25 °C) showed a maximum tensile stress greater than at 200 °C. For example, the maximum
 631 tensile stress of about 50 MPa could be generated at the surface of the unaltered granite. These
 632 values were sufficient to produce significant thermal cracking as observed by the measured
 633 properties and the images from X-ray CT (Fig. 13).

634 The stress propagation from the surface to the interior of the sample, was directly related to the
 635 preheating temperature and the number of cycles. For both test, there was a fatigue threshold, that
 636 was the number of cycles from which the damage affected similarly the whole sample and the
 637 measured values were maintained or varied only slightly due mainly to crack redistribution. During
 638 repeated heating cycles, rocks can exhibit a stress memory effect, or the so-called Kaiser effect
 639 (Kaiser, 1953) which indicates that in order to sustain damage, a material must be subjected to
 640 stresses greater than those it has already experienced. This characteristic can be observed in many
 641 EGS sites during forced fluid injection operations (Maurer et al., 2020) and also under heat stress in
 642 the laboratory in a wide variety of rock types (Lavrov, 2003). For example, Yong and Wang (1980)
 643 have shown that there may be a Kaiser effect on the Westerly Granite because during the heating
 644 process and at temperatures below the peak temperature of the previous cycle, very little acoustic
 645 emission occurred.

646

647 Figure 17 shows the parameter changes of quenching samples preheated at 200 °C and 400 °C with
 648 cycles. The damage variability was defined taking into account the initial standard deviation and the

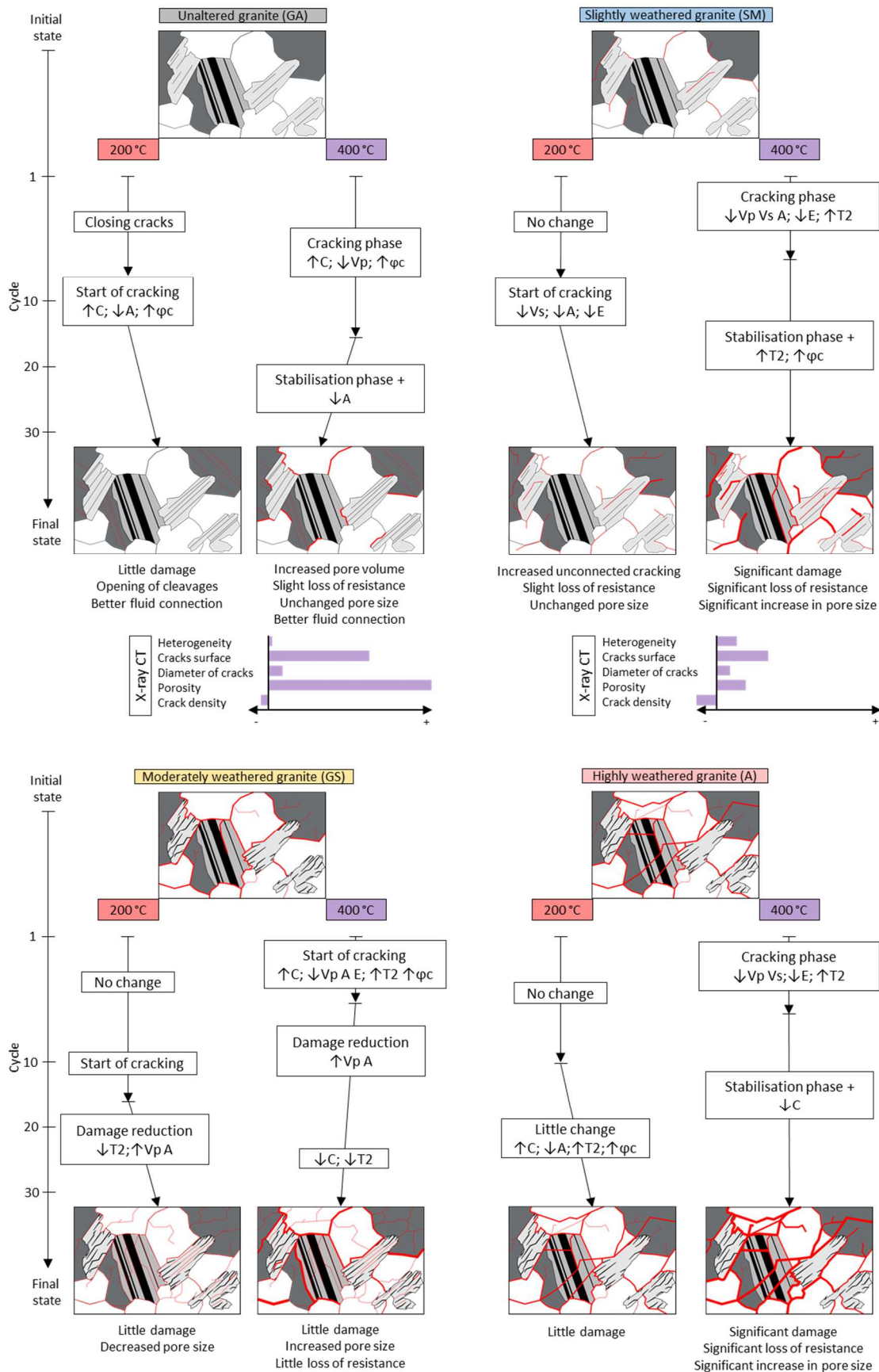
649 extreme values of all the granites. For rocks preheated to 200°C, at least between ten and fifteen
 650 cycles of quenching were necessary to reach the stress threshold or Kaiser Effect, although certain
 651 properties and granites revealed a continuous progression of microcracking until the end of the test.
 652 Meanwhile for those rocks preheated to 400°C, some definitive variations were observed from the
 653 very first cycle. The inadequacy of the thermal expansion coefficients of the different minerals
 654 prompted the generation of microcracks, causing significant damage to the granites (Jin et al., 2019;
 655 Sousa et al., 2005; Wu et al., 2019).



662 The unaltered granite GA, showed at 200°C, a progressive degradation until the end of the test. The
663 main parameters affected were the porosity and the capillarity that indicated an increase in the
664 volume and connectivity of the pores. The low initial porosity may influence the slight variation
665 related to the mechanical parameters. At 400°C, the change of these two parameters was enhanced
666 and accompanied by a noticeable increase in the microcracking as indirectly measured by
667 ultrasounds. In agreement with Zhu et al. (2020), V_p showed an approximately 40% reduction at 400
668 °C after 30 quenching cycles with a significant decrease from the very first cycle. This behaviour
669 agreed with the microcracking development observed in the figure 13, where X-ray CT also revealed
670 a propagation mainly in intergranular cracks that enhanced connectivity (Fig 18).

671

672 The weathered granites showed a variation in microstructure due to crack propagation and opening,
673 although without improving connectivity. The development of microcracking detected by ultrasound
674 parameters and also observed by X-ray CT revealed a widening and propagation of transgranular
675 microcracks that were not forcedly connected between them. For the three granites and both
676 temperatures, 200°C and 400°C, connected porosity and capillary coefficient hardly changed. At 200
677 °C, noticeable changes were measured after 10 cycles, followed by stabilization. Albero, the most
678 weathered granite hardly showed any variation. At 400°C, a strong decrease in the dynamic and
679 elastic parameters related to strength were measured from cycle 1 to 5. The small microcrack
680 network observed in feldspars and the widening of long intragranular cracks may experiment
681 readjustments during the rest of the cycles although without improving connectivity (Fig 18).



682

683 **Fig. 18: Synthesis of microstructural observations of the granites after quenching from 200°C and**
 684 **400°C. ↑: increase; ↓: decrease; C: capillary coefficient; Vp: P-wave propagation velocity; Vs: S-**

685 **wave propagation velocity; A: Amplitude coefficient; E: Young's modulus; T2: transverse relaxation**
686 **time and φ_c : Connected porosity.**

687 5.2. Damage evaluation and permeability

688 With increasing the crack density and increasing the number of cycles, cracks can penetrate more
689 easily, which improves the permeability. On the other hand, the strong thermal gradient generated
690 would tend to cause damage in the borehole.

691 Permeability is an important parameter that is generally used to describe the ability of the rock to
692 allow the flow of fluids through its pores. The permeability (k) was estimated from the
693 Schlumberger-Doll Research (SDR) equation (7), based on the Kozeny-Carmen equation, as indicated
694 in the following equation (Kenyon et al., 1988; Straley et al., 1997):

695

$$696 k = b\varphi^m(T2_{LM})^n \quad (7)$$

697

698 Where φ is the porosity, $T2_{LM}$ is the mean log of the T2 distribution, and b , m , and n are empirically
699 determined parameters. Each of the SDR parameters is expected to have a dependence on the
700 lithology.

701

702 The porosity exponent m is associated with the Archie's formation resistivity factor (Chang et al.,
703 1994). The exponent of the relaxation time n is associated with the grain size distribution (Dunn et
704 al., 1999). For consolidated materials, $m = 4$ and $n = 2$ are the most commonly reported values
705 (Knight et al., 2016; Ren et al., 2019). The constant b is considered to be dependent on the lithology
706 and is related to the surface relaxivity ρ . It represents a practical calibration parameter to take into
707 account these other properties independent of geological materials which are difficult to measure or
708 quantify to obtain the best possible match for predicting permeability (Maurer and Knight, 2016). In
709 petroleum applications, for $m = 4$ and $n = 2$, the standard value of b is $4 \text{ mD ms}^{-2} = 3.95 \times 10^{-9} \text{ m}^2 \cdot \text{s}^{-2}$
710 (Kenyon et al., 1995). We set these parameters for this study.

711

712 As indicated in section 5.1, the quenching cycles induce significant damage on the granite.

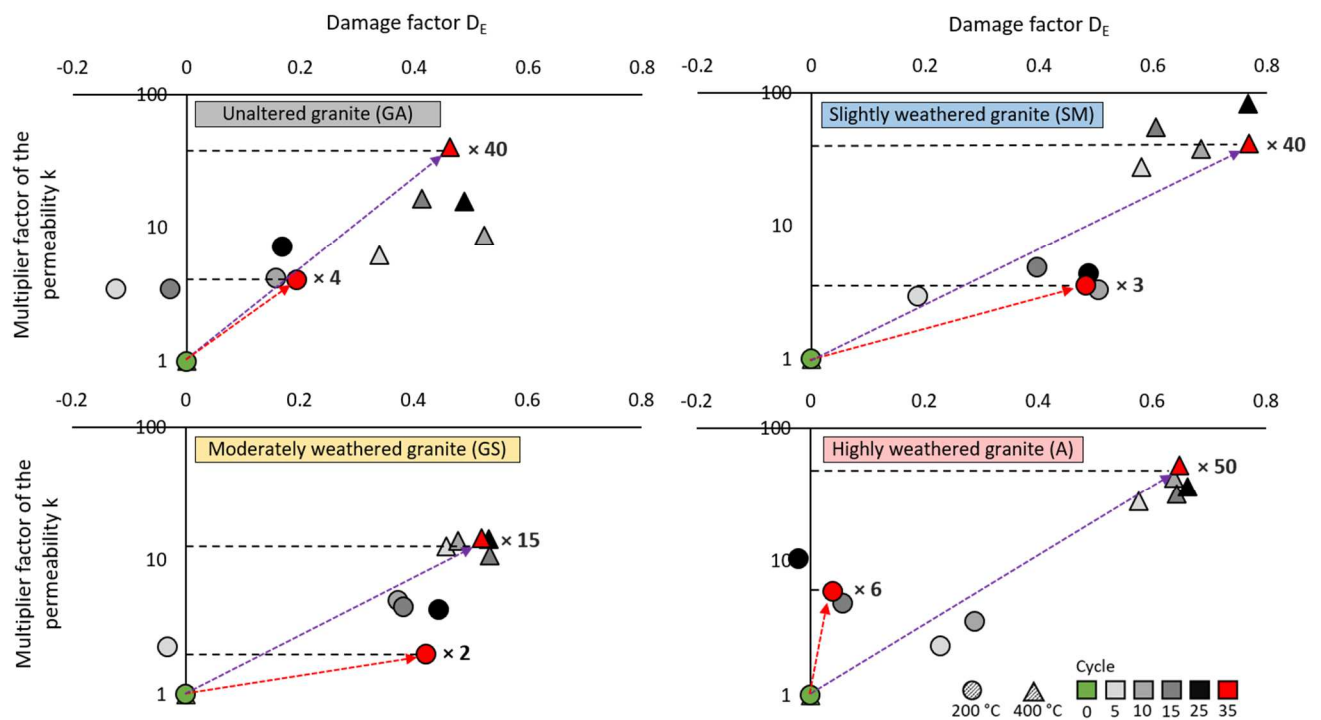
713 The thermal damage which is related to Young's modulus was thanks to the damage factor $D_E(T)$
714 (Guo et al., 2018; Sha et al., 2020; W. Zhang et al., 2018), indicated in the following equation:

$$715 D_E(T) = 1 - \frac{E_T}{E_0} \quad (8)$$

716 Where E_0 and E_T are the values of the modulus of elasticity at room temperature, and temperature T
717 (200°C - 400°C), respectively. The application of this calculation was carried out at the two treatment
718 temperatures and as a function of the number of cycles.

719

720 Figure 19 represents the evolution of the permeability k and the damage factor D_E as a function of
721 the number of cycles. For each cycle, the average value of three samples is given.



722

723 **Figure 19: Evolution of the permeability k and the damage factor D_E as a function of the number of**
724 **cycles. Samples preheated at 200 °C and 400 °C are represented by circles and triangles,**
725 **respectively. The red and purple arrows represent the direction of the evolution of the 2**
726 **parameters. The base of arrows is positioned on the average value of 3 initial samples and having**
727 **reached the average value of 3 samples of the final cycle.**

728 Thermally induced fractures have improved the permeability of all the samples after 35 cycles at
729 400 °C. The critical temperature for which the permeability of granite significantly increases (Zhao et
730 al., 2017) is set at 400 °C (Jin et al., 2019). Increasing crack density also leads to an increase in
731 damage factor (Feng et al., 2020; Guo et al., 2018; Sha et al., 2020). The changes of the Young's
732 modulus (E) were smaller during the quenching test at 200 °C than at 400 °C. At the end of the 35
733 cycles of quenching of the samples at 400 °C, E had decreased by 2.3, 1.6, 2.0, and 2.6 times that
734 values compared to the thermal cycling performed at 200 °C for A, GA, GS, and SM, respectively. If
735 rocks heated at 200 °C still showed variability between cycles, on the other hand at 400 °C, the main
736 changes were made during the first cycles.

737

738 At the end of the quenching tests, the permeability of the unaltered and slightly weathered granite
739 was improved by a factor of approximately 5 at 200 °C and by a factor of 40 at 400 °C. At the same
740 processing temperature, quenching showed more damage on the slightly weathered granite which
741 could be due to its larger grain size (Shao et al., 2014).

742 The permeability of the moderately weathered granite was less affected by the quenching.
743 Quenching cycles closed induced fractures after the first cycles following volumetric expansion
744 (Barton, 2007), reducing hydraulic connections.

745 The 50-fold increase in permeability occurred after the first 5 thermal cycles for highly weathered
746 granite (A) and was accompanied by a significant damage unlike quenching at 200 °C. This suggests
747 that microcracks dominated the flow pathways through the sample.

748 5.3. Chemical analysis of fluids

749 The experimental fluids showed chemical element concentrations indicating signs of alteration of
750 minerals present in the granite. The main reactive minerals were alkaline feldspars and clays. The
751 increase of elements K and Al in the resulting water could be produced by the gradual alteration of
752 alkali feldspar. In general, these 2 main elements resulting from water-granite rock interactions
753 come mainly from the alteration of clays. They would be introduced into the fluid phase by the
754 degradation of the surface of clay minerals such as smectite, illite, or kaolinite. K, Mg, Mn, Ti in the
755 fluid came from biotite during the opening of the mica cleavages with temperature (Vazquez et al.,
756 2015).

757 Ca can be found in the saturating fluid by the degradation and dissolution of plagioclases (Wogelius
758 et al., 2020). Indeed, calcite-mineralised, transgranular, and intra-granular microcracks were
759 particularly frequent in plagioclase crystals, which generally show exsolution or zonation figures
760 during their crystallisation. The composition of the water showed a slight increase in Fe. This
761 enrichment may be due to iron degradation from biotite (Vazquez et al., 2016).

762 The K-feldspar-water interactions must lead to an increase in Al, Si, K, and Na in the fluid from 200 °C
763 (Drüppel et al., 2020). Based on the ICP data, the increase of the concentration of all the mentioned
764 elements with the number of cycles for the two quenching tests could be attributed to the
765 dissolution or mechanical deterioration of K-feldspar. It was noted that this dissolution kinetics was
766 greater for rocks preheated at 400 °C. Feldspar crystals observed on X-ray CT showed intergranular
767 and intragranular cracking.

768 The unaltered granite showed the highest K content during the final cycle at 400 °C. An evident
769 intragranular microcrack was observed in K-feldspar which can go as far as coalescing with other
770 intergranular microcracks (Fig. 13). However, this high content can be interpreted by the high
771 proportion of K-feldspar compared to other granites.

772 While the observed chemical alterations were independent of physical processes, minerals that
773 underwent more physical deterioration also suffered more chemical alteration.

774

775 5.4. Potential application of quenching in Enhanced Geothermal System (EGS) projects

776 Quenching of granite formations is closely linked to the implementation and the development of
777 EGS projects. Stimulation of a rock reservoir by hydraulic fracturing from water at room temperature
778 is often adopted to improve the porosity and permeability of the rock. The permeability obtained in
779 this study was an estimate calculated from the NMR petrophysical data, used specifically as a
780 comparison between four granites, while capillary imbibition testing was used as an estimator of
781 rock degradation and conductivity index. It is inversely linked to the durability of stone (Benavente
782 et al., 2004; Çelik and Kaçmaz, 2016; Fronteau, 2000; Sengun et al., 2014). Knowing the movement
783 of water inside the rock is a simple way to assess the porosity of the rock (Fronteau et al., 2010).
784 Benavente et al. (2015) show a strong relationship between the coefficient of water absorption by
785 capillarity and water permeability.

786 The experimental results showed that whatever the granite tested, the effect of the thermal shock
787 increased the permeability estimated by NMR and that the connectivity of the water by capillary
788 imbibition could vary according to the type of granite.

789 In addition, the higher the temperature of the formation, the more the thermal stimulation will
790 create cracks in the formation. The irreversible cracking stress was not always at 200 ° C to generate
791 the Kaiser effect, as for the sound granite GA. As a Kaiser effect was observed during heating to 400 °
792 C and rapid cooling, it can be concluded that the improvement of the permeability around the
793 geothermal wells would be effective from the first cycles, but renewing the thermal stimulation
794 would not be more beneficial. Indeed, heating the rock in repeated cycles without inducing cracking
795 could induce a closure of the pre-existing microcracks with the expansion of the rock matrix.
796 Thermal stimulation can be used to rapidly increase the permeability of rocks and thermal fatigue
797 could potentially strengthen the rock mass or to remobilize the porous network.

798 The experimental data also showed that as the quenching progressed, fracturing increased which
799 would lead to a decrease of the mechanical properties. Transcribed to the geothermal system, this
800 observation means that if the thermal stress exceeds the equilibrium threshold of the surrounding
801 deep rock system, zones of fragility could be created. The mechanisms involved during hydraulic
802 stimulation could locally modify the stresses that could be at the origin of microseismicity, that may
803 cause damage to local populations. Between June and July 2000, a hydraulic stimulation experiment
804 took place at the EGS geothermal site in Soultz-sous-Forêts (Alsace, France) and more than 7,200
805 microseismic events were located in the range of magnitude -0.9 to 2.6 (Cuenot et al., 2008). In
806 2006, the geothermal energy project in Basel (Switzerland) was stopped due to a seismic event of
807 magnitude greater than 2.0 which caused some damage to buildings. Therefore, during hydraulic
808 fracturing, it is necessary to ensure that the quenching only reaches the area dedicated to fracturing.

809 It is therefore necessary to implement technologies such as thermal insulation of pipelines (Shen et
810 al., 2020).

811 In this study, we focused on the effect of thermal cycling on the petrophysical properties of granite
812 after quenching and hoped to contribute to the stability of boreholes when exploiting deep
813 geothermal energy. All the tests were performed in an unconfined condition. However, geothermal
814 reservoir rocks are subject to confinement pressure. Therefore, the behaviour of granite after
815 quenching under these conditions requires further studies.

816 6. Conclusion

817 The study of quenching damage is essential to understand the fracturing on the permeability of the
818 reservoir and therefore the life of a geothermal installation. In this work, the thermal shock
819 behaviour of four granites with different initial properties was followed. From the results of the
820 study, the following conclusions are drawn:

821 Strong correlations between the coefficient of capillarity, the P- S-wave propagation velocity,
822 Young's modulus, and the porosity have been established. The size of the cracks measured with the
823 NMR showed an increased with the number of cycles. Due to the different crystal structure of the 4
824 granites, the thermal stress limit threshold and the cracking morphology is different. If crack
825 openings or closings occurred in weathered granites during thermal shocks, the size of the
826 microcracks did not change in the sound granite but their density did. The change if the predicted
827 permeability was a direct consequence of the propagation of microcracks induced by the strong
828 gradient during quenching tests.

829 A single cycle of a thermal shock for rocks preheated at 400 °C prompted more damage than after 35
830 cycles at 200 °C. The propagation of pre-existing cracks was observed with X-ray CT and the
831 enlargement of the size of the cracks with NMR, especially for granites with the smallest initial T2
832 value (A and SM).

833 In the case of rapid quenching from 400 °C, intragranular microcracks within the K-feldspar
834 propagated throughout the low initial porosity granites (the unaltered GA and the slightly weathered
835 SM). For these less weathered granites, the expansion and contraction of the minerals lead to
836 greater damage inside the crystals. The increase of connectivity improves the permeability while the
837 more weathered granites experimented an increase of microcracking with less connectivity.

838 The chemical analysis of the fluids used for cooling served as clues of the mineralogical alteration
839 and allowed the alteration processes to be evaluated. The water-granite rock interaction showed the
840 dissolution of K-feldspar, plagioclase, and the degradation of clays, leading to an enrichment mainly
841 in K, Na, and Ca in solution.

842

843 **Declaration of Competing Interest:**

844 The authors report no declarations of interest.

845 **Acknowledgments:**

846 This work was carried out within the framework of the FLUTE Project. We would like to express our
847 deep gratitude to our partners from the University of Reims Champagne-Ardenne (France), La
848 Région Grand Est and Regional Government of Comunidad Valenciana (Spain) [grant number
849 AICO/2020/175], for their kind scientific collaboration and participation in the development of this
850 project.

851 **Reference**

852

- 853 Albissin, M.C., Sirieys, P., 1989. Thermal Deformability of Rocks: Relation to Rock Structure.
854 Presented at the ISRM International Symposium, International Society for Rock Mechanics
855 and Rock Engineering.
- 856 Alt-Epping, P., Diamond, L.W., Häring, M.O., Ladner, F., Meier, D.B., 2013. Prediction of water–rock
857 interaction and porosity evolution in a granitoid-hosted enhanced geothermal system, using
858 constraints from the 5km Basel-1 well. *Applied Geochemistry* 38, 121–133.
859 <https://doi.org/10.1016/j.apgeochem.2013.09.006>
- 860 Baldeyrou-Bailly, A., Surma, F., Fritz, B., 2004. Geophysical and mineralogical impacts of fluid
861 injection in a geothermal system: the Hot Fractured Rock site at Soultz-sous-Forêts, France.
862 *Geological Society, London, Special Publications* 236, 355–367.
863 <https://doi.org/10.1144/GSL.SP.2004.236.01.20>
- 864 Barton, N., 2007. Thermal over-closure of joints and rock masses and implications for HLW
865 repositories. *Proc. of 11th ISRM Congress* 109–116.
- 866 Benavente, D., Galiana-Merino, J.J., Pla, C., Martínez-Martínez, J., Crespo-Jimenez, D., 2020.
867 Automatic detection and characterisation of the first P- and S-wave pulse in rocks using
868 ultrasonic transmission method. *Engineering Geology* 266, 105474.
869 <https://doi.org/10.1016/j.enggeo.2020.105474>
- 870 Benavente, D., García del Cura, M.A., Fort, R., Ordóñez, S., 2004. Durability estimation of porous
871 building stones from pore structure and strength. *Engineering Geology* 74, 113–127.
872 <https://doi.org/10.1016/j.enggeo.2004.03.005>
- 873 Benavente, D., Lock, P., Ángeles García Del Cura, M., Ordóñez, S., 2002. Predicting the Capillary
874 Imbibition of Porous Rocks from Microstructure. *Transport in Porous Media* 49, 59–76.
875 <https://doi.org/10.1023/A:1016047122877>
- 876 Benavente, D., Pla, C., Cueto, N., Galvañ, S., Martínez-Martínez, J., García-del-Cura, M.A., Ordóñez,
877 S., 2015. Predicting water permeability in sedimentary rocks from capillary imbibition and
878 pore structure. *Engineering Geology* 195, 301–311.
879 <https://doi.org/10.1016/j.enggeo.2015.06.003>
- 880 Bérard, T., Cornet, F.H., 2003. Evidence of thermally induced borehole elongation: a case study at
881 Soultz, France. *International Journal of Rock Mechanics and Mining Sciences, Special Issue of*
882 *the IJRMMS: Rock Stress Estimation ISRM Suggested Methods and Associated Supporting*
883 *Papers* 40, 1121–1140. [https://doi.org/10.1016/S1365-1609\(03\)00118-7](https://doi.org/10.1016/S1365-1609(03)00118-7)
- 884 Berest, P., Vouille, G., 1988. *Notions de base de la thermomécanique : La Thermomécanique des*
885 *Roches. Manuels et Méthodes, Brgm. ed.*

886 Breede, K., Dzebisashvili, K., Liu, X., Falcone, G., 2013. A systematic review of enhanced (or
887 engineered) geothermal systems: past, present and future. *Geothermal Energy* 1, 4.
888 <https://doi.org/10.1186/2195-9706-1-4>

889 Cai, J., Yu, B., 2011. A Discussion of the Effect of Tortuosity on the Capillary Imbibition in Porous
890 Media. *Transp Porous Med* 89, 251–263. <https://doi.org/10.1007/s11242-011-9767-0>

891 Çelik, M.Y., Kaçmaz, A.U., 2016. The investigation of static and dynamic capillary by water absorption
892 in porous building stones under normal and salty water conditions. *Environmental Earth*
893 *Sciences* 75, 307.

894 Chaki, S., Takarli, M., Agbodjan, W.P., 2008. Influence of thermal damage on physical properties of a
895 granite rock: Porosity, permeability and ultrasonic wave evolutions. *Construction and*
896 *Building Materials* 22, 1456–1461. <https://doi.org/10.1016/j.conbuildmat.2007.04.002>

897 Chang, D., Vinegar, H.J., Morriss, C., Straley, C., 1994. Effective Porosity, Producing Fluid And
898 Permeability In Carbonates From Nmr Logging. Presented at the SPWLA 35th Annual Logging
899 Symposium, OnePetro.

900 Cuenot, N., Dorbath, C., Dorbath, L., 2008. Analysis of the Microseismicity Induced by Fluid Injections
901 at the EGS Site of Soultz-sous-Forêts (Alsace, France): Implications for the Characterization of
902 the Geothermal Reservoir Properties. *Pure and Applied Geophysics* 165, 797–828.
903 <https://doi.org/10.1007/s00024-008-0335-7>

904 David, C., Menéndez, B., Darot, M., 1999. Influence of stress-induced and thermal cracking on
905 physical properties and microstructure of La Peyratte granite. *International Journal of Rock*
906 *Mechanics and Mining Sciences* 36, 433–448. [https://doi.org/10.1016/S0148-](https://doi.org/10.1016/S0148-9062(99)00010-8)
907 [9062\(99\)00010-8](https://doi.org/10.1016/S0148-9062(99)00010-8)

908 Dong, Z., Sun, Q., Zhang, W., Xu, C., 2020. Thermal damage of granite after thermal shock cycle.
909 *Géotechnique Letters* 10, 168–173. <https://doi.org/10.1680/jgele.19.00062>

910 Drüppel, K., Stober, I., Grimmer, J.C., Mertz-Kraus, R., 2020. Experimental alteration of granitic rocks:
911 Implications for the evolution of geothermal brines in the Upper Rhine Graben, Germany.
912 *Geothermics* 88, 101903. <https://doi.org/10.1016/j.geothermics.2020.101903>

913 Dunn, K., LaTorraca, G.A., Bergman, D.J., 1999. Permeability relation with other petrophysical
914 parameters for periodic porous media. *GEOPHYSICS* 64, 470–478.
915 <https://doi.org/10.1190/1.1444552>

916 Dwivedi, R.D., Goel, R.K., Prasad, V.V.R., Sinha, A., 2008. Thermo-mechanical properties of Indian
917 and other granites. *International Journal of Rock Mechanics and Mining Sciences* 45, 303–
918 315. <https://doi.org/10.1016/j.ijrmms.2007.05.008>

919 Fan, L., Gao, J., Du, X., Wu, Z., 2020. Spatial gradient distributions of thermal shock-induced damage
920 to granite. *Journal of Rock Mechanics and Geotechnical Engineering* 12, 917–926.
921 <https://doi.org/10.1016/j.jrmge.2020.05.004>

922 Fan, L.F., Gao, J.W., Wu, Z.J., Yang, S.Q., Ma, G.W., 2018. An investigation of thermal effects on
923 micro-properties of granite by X-ray CT technique. *Applied Thermal Engineering* 140, 505–
924 519. <https://doi.org/10.1016/j.applthermaleng.2018.05.074>

925 Farias, P., Gallastegui, G., González Lodeiro, F., Marquínez, J., Martín Parra, L.M., Martínez Catalán,
926 J.R., Pablo Maciá, J. de, Rodríguez Fernández, L.R., 1987. Aportaciones al conocimiento de la
927 litoestratigrafía y estructura de Galicia Central. *Memórias da Faculdade de Ciências,*
928 *Universidade do Porto* 1, 411–431.

929 Feng, G., Wang, X., Wang, M., Kang, Y., 2020. Experimental investigation of thermal cycling effect on
930 fracture characteristics of granite in a geothermal-energy reservoir. *Engineering Fracture*
931 *Mechanics* 235, 107180. <https://doi.org/10.1016/j.engfracmech.2020.107180>

932 Fleury, M., 1998. Caractérisation de structures poreuses par relaxométrie RMN. *Rev. Inst. Fr. Pét.* 53,
933 489–493. <https://doi.org/10.2516/ogst:1998041>

934 Flores, M., Davies, D.R., Couples, G.D., Palsson, B., 2005. Stimulation of geothermal wells, can we
935 afford it? Presented at the World Geothermal Congress 2005.

936 Fredrich, J.T., Wong, T., 1986. Micromechanics of thermally induced cracking in three crustal rocks.
937 Journal of Geophysical Research: Solid Earth 91, 12743–12764.
938 <https://doi.org/10.1029/JB091iB12p12743>

939 Freire-Lista, D.M., Fort, R., Varas-Muriel, M.J., 2016. Thermal stress-induced microcracking in
940 building granite. Engineering Geology 206, 83–93.
941 <https://doi.org/10.1016/j.enggeo.2016.03.005>

942 Fronteau, G., 2000. Comportements tégénétiques des principaux calcaires de Champagne-
943 Ardenne : en relation avec leur facies de dépôt et leur sequençage diagénétique (These de
944 doctorat). Reims.

945 Fronteau, G., Moreau, C., Thomachot-Schneider, C., Barbin, V., 2010. Variability of some Lutetian
946 building stones from the Paris Basin, from characterisation to conservation. Engineering
947 Geology, Natural stones for historical monuments, testing, durability and provenance 115,
948 158–166. <https://doi.org/10.1016/j.enggeo.2009.08.001>

949 Gautam, P.K., Verma, A.K., Jha, M.K., Sharma, P., Singh, T.N., 2018. Effect of high temperature on
950 physical and mechanical properties of Jalore granite. Journal of Applied Geophysics 159,
951 460–474. <https://doi.org/10.1016/j.jappgeo.2018.07.018>

952 Géraud, Y., 1994. Variations of connected porosity and inferred permeability in a thermally cracked
953 granite. Geophysical Research Letters 21, 979–982. <https://doi.org/10.1029/94GL00642>

954 Géraud, Y., Gaviglio, P., 1990. Textural changes in granites submitted to artificial heating: porosity
955 and density variations as functions of the temperature. Comptes Rendus de l'Academie des
956 Sciences. Serie 2 310, 1681–1686.

957 Géraud, Y., Tournier, B., Mazerolle, F., 1999. Detection of porosity and mineralogical variations in
958 geological materials: radiological density measured by CT scan. Proceedings of the
959 International Symposium on Imaging Applications in Geology Geovision 99, 109–112.

960 Glover, P.W.J., Baud, P., Darot, M., Meredith, P.G., Boon, S.A., LeRavalec, M., Zoussi, S., Reuschlé, T.,
961 1995. α/β phase transition in quartz monitored using acoustic emissions. Geophysical
962 Journal International 120, 775–782. <https://doi.org/10.1111/j.1365-246X.1995.tb01852.x>

963 Gómez-Heras, M., Smith, B.J., Fort, R., 2006. Surface temperature differences between minerals in
964 crystalline rocks: Implications for granular disaggregation of granites through thermal
965 fatigue. Geomorphology 78, 236–249. <https://doi.org/10.1016/j.geomorph.2005.12.013>

966 Griffiths, L., Lengline, O., Heap, M., Baud, P., Schmittbuhl, J., 2018. Thermal Cracking in Westerly
967 Granite Monitored Using Direct Wave Velocity, Coda Wave Interferometry, and Acoustic
968 Emissions. Journal of Geophysical Research: Solid Earth 123, 2246–2261.
969 <https://doi.org/10.1002/2017JB015191>

970 Guo, L.-L., Zhang, Y.-B., Zhang, Y.-J., Yu, Z.-W., Zhang, J.-N., 2018. Experimental investigation of
971 granite properties under different temperatures and pressures and numerical analysis of
972 damage effect in enhanced geothermal system. Renewable Energy 126, 107–125.
973 <https://doi.org/10.1016/j.renene.2018.02.117>

974 Hall, K., André, M.-F., 2003. Rock thermal data at the grain scale: applicability to granular
975 disintegration in cold environments. Earth Surface Processes and Landforms 28, 823–836.
976 <https://doi.org/10.1002/esp.494>

977 Hammecker, C., Jeannette, D., 1994. Modelling the capillary imbibition kinetics in sedimentary rocks:
978 Role of petrographical features. Transp Porous Med 17, 285–303.
979 <https://doi.org/10.1007/BF00613588>

980 Hammecker, C., Mertz, J.-D., Fischer, C., Jeannette, D., 1993. A geometrical model for numerical
981 simulation of capillary imbibition in sedimentary rocks. Transp Porous Med 12, 125–141.
982 <https://doi.org/10.1007/BF00616976>

983 Homand, F., Duffaut, P., Bérest, P., Billiaux, D., Boulon, M., Cornet, F., David, C., Durville, J.L., Gentier,
984 S., Giraud, A., Ghoreychi, M., Henry, J.P., Kondo, D., Londe, P., Pellet, F., Piguet, J.P., Sarda,
985 J.P., Shao, J.F., Souley, M., 2000. Manuel de mécanique des roches - tome 1 Fondements,
986 Ecole des Mines de Paris.

987 Isaka, B.L.A., Gamage, R.P., Rathnaweera, T.D., Perera, M.S.A., Chandrasekharam, D., Kumari,
988 W.G.P., 2018. An Influence of Thermally-Induced Micro-Cracking under Cooling Treatments:
989 Mechanical Characteristics of Australian Granite. *Energies* 11, 1338.
990 <https://doi.org/10.3390/en11061338>

991 Isaka, B.L.A., Ranjith, P.G., Rathnaweera, T.D., Perera, M.S.A., Kumari, W.G.P., 2019. Influence of
992 long-term operation of supercritical carbon dioxide based enhanced geothermal system on
993 mineralogical and microstructurally-induced mechanical alteration of surrounding rock mass.
994 *Renewable Energy* 136, 428–441. <https://doi.org/10.1016/j.renene.2018.12.104>

995 Jin, P., Hu, Y., Shao, J., Zhao, G., Zhu, X., Li, C., 2019. Influence of different thermal cycling treatments
996 on the physical, mechanical and transport properties of granite. *Geothermics* 78, 118–128.
997 <https://doi.org/10.1016/j.geothermics.2018.12.008>

998 Junique, T., Vázquez, P., Géraud, Y., Thomachot-Schneider, C., Sidibé, H., 2021. Microstructural
999 evolution of granitic stones exposed to different thermal regimes analysed by infrared
1000 thermography. *Engineering Geology* 286, 106057.
1001 <https://doi.org/10.1016/j.enggeo.2021.106057>

1002 Kaiser, J., 1953. Erkenntnisse und Folgerungen aus der Messung von Geräuschen bei
1003 Zugbeanspruchung von metallischen Werkstoffen. *Archiv für das Eisenhüttenwesen* 24, 43–
1004 45. <https://doi.org/10.1002/srin.195301381>

1005 Kant, M.A., Ammann, J., Rossi, E., Madonna, C., Höser, D., Rohr, P.R. von, 2017. Thermal properties
1006 of Central Aare granite for temperatures up to 500°C: Irreversible changes due to thermal
1007 crack formation. *Geophysical Research Letters* 44, 771–776.
1008 <https://doi.org/10.1002/2016GL070990>

1009 Keating, K., Knight, R., 2006. A laboratory study to determine the effect of iron oxides on proton
1010 NMR measurements. *GEOPHYSICS* 72, E27–E32. <https://doi.org/10.1190/1.2399445>

1011 Kenyon, B., Kleinberg, R., Straley, C., Gubelin, G., Morriss, C., 1995. Nuclear magnetic resonance
1012 imaging - technology for the 21st century. *Oilfield Review* 7, 19–33.

1013 Kenyon, W.E., Day, P.I., Straley, C., Willemsen, J.F., 1988. A Three-Part Study of NMR Longitudinal
1014 Relaxation Properties of Water-Saturated Sandstones. *SPE Form Eval* 3, 622–636.
1015 <https://doi.org/10.2118/15643-PA>

1016 Kim, K., Kemeny, J., Nickerson, M., 2014. Effect of Rapid Thermal Cooling on Mechanical Rock
1017 Properties. *Rock Mech Rock Eng* 47, 2005–2019. <https://doi.org/10.1007/s00603-013-0523-3>

1018 3

1019 Knight, R., Walsh, D.O., Butler, J.J., Grunewald, E., Liu, G., Parsekian, A.D., Reboulet, E.C., Knobbe, S.,
1020 Barrows, M., 2016. NMR Logging to Estimate Hydraulic Conductivity in Unconsolidated
1021 Aquifers. *Groundwater* 54, 104–114. <https://doi.org/10.1111/gwat.12324>

1022 Kovač, K., Moore, J., McCulloch, J., Ekart, D., 2004. Geology and Mineral Paragenesis Study Within
1023 the Coso-EGS Project. Presented at the Twenty-Ninth Workshop on Geothermal Reservoir
1024 Engineering Stanford University, Stanford, California.

1025 Kumari, W.G.P., Ranjith, P.G., Perera, M.S.A., Chen, B.K., 2018. Experimental investigation of
1026 quenching effect on mechanical, microstructural and flow characteristics of reservoir rocks:
1027 Thermal stimulation method for geothermal energy extraction. *Journal of Petroleum Science*
1028 *and Engineering* 162, 419–433. <https://doi.org/10.1016/j.petrol.2017.12.033>

1029 Kumari, W.G.P., Ranjith, P.G., Perera, M.S.A., Chen, B.K., Abdulagatov, I.M., 2017a. Temperature-
1030 dependent mechanical behaviour of Australian Strathbogie granite with different cooling
1031 treatments. *Engineering Geology* 229, 31–44. <https://doi.org/10.1016/j.enggeo.2017.09.012>

1032 Kumari, W.G.P., Ranjith, P.G., Perera, M.S.A., Shao, S., Chen, B.K., Lashin, A., Arifi, N.A.,
1033 Rathnaweera, T.D., 2017b. Mechanical behaviour of Australian Strathbogie granite under in-
1034 situ stress and temperature conditions: An application to geothermal energy extraction.
1035 *Geothermics* 65, 44–59. <https://doi.org/10.1016/j.geothermics.2016.07.002>

- 1036 Lam dos Santos, J.P., Rosa, L.G., Amaral, P.M., 2011. Temperature effects on mechanical behaviour
 1037 of engineered stones. *Construction and Building Materials* 25, 171–174.
 1038 <https://doi.org/10.1016/j.conbuildmat.2010.06.042>
- 1039 Lavrov, A., 2003. The Kaiser effect in rocks: principles and stress estimation techniques. *International*
 1040 *Journal of Rock Mechanics and Mining Sciences* 40, 151–171.
 1041 [https://doi.org/10.1016/S1365-1609\(02\)00138-7](https://doi.org/10.1016/S1365-1609(02)00138-7)
- 1042 Le Maitre, R.W. (Ed.), 2002. *Igneous Rocks: A Classification and Glossary of Terms:*
 1043 *Recommendations of the International Union of Geological Sciences Subcommission on the*
 1044 *Systematics of Igneous Rocks*, 2nd ed. Cambridge University Press, Cambridge.
 1045 <https://doi.org/10.1017/CBO9780511535581>
- 1046 Li, C., Hu, Y., Meng, T., Jin, P., Zhao, Z., Zhang, C., 2020. Experimental study of the influence of
 1047 temperature and cooling method on mechanical properties of granite: Implication for
 1048 geothermal mining. *Energy Science & Engineering* 8, 1716–1728.
 1049 <https://doi.org/10.1002/ese3.627>
- 1050 Lin, W., 2002. Permanent strain of thermal expansion and thermally induced microcracking in Inada
 1051 granite. *Journal of Geophysical Research: Solid Earth* 107, ECV 3-1-ECV 3-16.
 1052 <https://doi.org/10.1029/2001JB000648>
- 1053 Liu, C., Deng, H., Wang, Y., Lin, Y., Zhao, H., 2017. Time-Varying Characteristics of Granite
 1054 Microstructures after Cyclic Dynamic Disturbance Using Nuclear Magnetic Resonance.
 1055 *Crystals* 7, 306. <https://doi.org/10.3390/cryst7100306>
- 1056 Lutz, S., Robertson-Tait, A., Morris, C., 2004. Stratigraphic relationships in Mesozoic basement rocks
 1057 at the Desert Peak East EGS area, Nevada. Presented at the Twenty-Ninth Workshop on
 1058 Geothermal Reservoir Engineering Stanford, University, Stanford, California.
- 1059 Marshall, V., van Zyl, J., Bryan, S., Uysal, T., Gasparon, M., 2010. Comparative petrology and
 1060 geochemistry of high heat-producing granites in Australia and Europe, in: Weber, R.D.,
 1061 Gurgenci, H. (Eds.), *Proceedings of the 2010 Australian Geothermal Energy Conference.*
 1062 Presented at the Australian Geothermal Energy Conference, Geoscience Australia, Australia,
 1063 pp. 41–47.
- 1064 Martínez-Martínez, J., Benavente, D., García-del-Cura, M.A., 2011. Spatial attenuation: The most
 1065 sensitive ultrasonic parameter for detecting petrographic features and decay processes in
 1066 carbonate rocks. *Engineering Geology* 119, 84–95.
 1067 <https://doi.org/10.1016/j.enggeo.2011.02.002>
- 1068 Maurer, J., Knight, R., 2016. Models and methods for predicting hydraulic conductivity in near-
 1069 surface unconsolidated sediments using nuclear magnetic resonance. *GEOPHYSICS* 81,
 1070 D503–D518. <https://doi.org/10.1190/geo2015-0515.1>
- 1071 Maurer, V., Gaucher, E., Grunberg, M., Koepke, R., Pestourie, R., Cuenot, N., 2020. Seismicity
 1072 induced during the development of the Rittershoffen geothermal field, France. *Geothermal*
 1073 *Energy* 8. <https://doi.org/10.1186/s40517-020-0155-2>
- 1074 NF EN 1925, 1999. Méthodes d'essai pour pierres naturelles - Détermination du coefficient
 1075 d'absorption d'eau par capillarité.
- 1076 NF EN 1936, 2007. Natural stone test methods-Determination of real density and apparent density
 1077 and of total and open porosity.
- 1078 Olasolo, P., Juárez, M.C., Morales, M.P., D'Amico, S., Liarte, I.A., 2016. Enhanced geothermal systems
 1079 (EGS): A review. *Renewable and Sustainable Energy Reviews* 56, 133–144.
 1080 <https://doi.org/10.1016/j.rser.2015.11.031>
- 1081 Ren, S., Parsekian, A.D., Zhang, Y., Carr, B.J., 2019. Hydraulic Conductivity Calibration of Logging NMR
 1082 in a Granite Aquifer, Laramie Range, Wyoming. *Groundwater* 57, 303–319.
 1083 <https://doi.org/10.1111/gwat.12798>
- 1084 Reuschlé, T., Gbaguidi Haore, S., Darot, M., 2006. The effect of heating on the microstructural
 1085 evolution of La Peyratte granite deduced from acoustic velocity measurements. *Earth and*
 1086 *Planetary Science Letters* 243, 692–700. <https://doi.org/10.1016/j.epsl.2006.01.038>

1087 Roels, S., Carmeliet, J., Hens, H., Elsen, J., 2000. Microscopic analysis of imbibition processes in oolitic
1088 limestone. *Geophysical Research Letters* 27, 3533–3536.
1089 <https://doi.org/10.1029/1999GL008471>

1090 Schmidt, R.B., Bucher, K., Stober, I., 2018. Experiments on granite alteration under geothermal
1091 reservoir conditions and the initiation of fracture evolution. *European Journal of Mineralogy*
1092 30, 899–916. <https://doi.org/10.1127/ejm/2018/0030-2771>

1093 Sengun, N., Demirdag, S., Akbay, D., Ugur, I., Altindag, R., Akbulut, A., 2014. Investigation of the
1094 relationships between capillary water absorption coefficients and other rock properties of
1095 some natural stones, V, in: *Global Stone Congress*. pp. 22–25.

1096 Sepúlveda, J., Arancibia, G., Molina, E., Gilbert, J.P., Duda, M., Browning, J., Roquer, T., Morata, D.,
1097 Ahrens, B., Bracke, R., 2020. Thermo-mechanical behavior of a granodiorite from the Liquiñe
1098 fractured geothermal system (39°S) in the Southern Volcanic Zone of the Andes.
1099 *Geothermics* 87, 101828. <https://doi.org/10.1016/j.geothermics.2020.101828>

1100 Sha, S., Rong, G., Chen, Z., Li, B., Zhang, Z., 2020. Experimental Evaluation of Physical and Mechanical
1101 Properties of Geothermal Reservoir Rock after Different Cooling Treatments. *Rock Mech*
1102 *Rock Eng* 53, 4967–4991. <https://doi.org/10.1007/s00603-020-02200-5>

1103 Shao, S.S., Wasantha, P.L., Ranjith, P.G., Chen, B., 2014. Effect of cooling rate on the mechanical
1104 behavior of heated Strathbogie granite with different grain sizes. *International Journal of*
1105 *Rock Mechanics & Mining Sciences* 70, 381–387.
1106 <https://doi.org/10.1016/j.ijrmms.2014.04.003>

1107 Shen, Y., Hou, X., Yuan, J., Xu, Z., Hao, J., Gu, L., Liu, Z., 2020. Thermal deterioration of high-
1108 temperature granite after cooling shock: multiple-identification and damage mechanism.
1109 *Bull Eng Geol Environ* 79, 5385–5398. <https://doi.org/10.1007/s10064-020-01888-7>

1110 Siratovich, P., Sass, I., Homuth, S., Bjornsson, A., 2011. Thermal Stimulation of Geothermal
1111 Reservoirs and Laboratory Investigation of Thermally Induced Fractures. *Transactions -*
1112 *Geothermal Resources Council* 35, 1529–1535.

1113 Siratovich, P.A., Heap, M.J., Villeneuve, M.C., Cole, J.W., Kennedy, B.M., Davidson, J., Reuschlé, T.,
1114 2016. Mechanical behaviour of the Rotokawa Andesites (New Zealand): Insight into
1115 permeability evolution and stress-induced behaviour in an actively utilised geothermal
1116 reservoir. *Geothermics* 64, 163–179. <https://doi.org/10.1016/j.geothermics.2016.05.005>

1117 Siratovich, P.A., Villeneuve, M.C., Cole, J.W., Kennedy, B.M., Bégué, F., 2015. Saturated heating and
1118 quenching of three crustal rocks and implications for thermal stimulation of permeability in
1119 geothermal reservoirs. *International Journal of Rock Mechanics and Mining Sciences* 80,
1120 265–280. <https://doi.org/10.1016/j.ijrmms.2015.09.023>

1121 Sousa, L.M.O., Suárez del Río, L.M., Calleja, L., Ruiz de Argandoña, V.G., Rey, A.R., 2005. Influence of
1122 microfractures and porosity on the physico-mechanical properties and weathering of
1123 ornamental granites. *Engineering Geology* 77, 153–168.
1124 <https://doi.org/10.1016/j.enggeo.2004.10.001>

1125 Straley, C., Rossini, D., Vinegar, H., Tutunjian, P., Morriss, C., 1997. Core Analysis By Low-field Nmr.
1126 *The Log Analyst* 38.

1127 Stussi, J.-M., Cheilietz, A., Royer, J.-J., Chervremont, P., Feraud, G., 2002. The hidden monzogranite
1128 of Soultz-sous-Forêts (Rhine Graben, France). *Mineralogy, petrology and genesis. Géol. Fr*
1129 45–64.

1130 Surma, F., Geraud, Y., 2003. Porosity and Thermal Conductivity of the Soultz-sous-Forêts Granite.
1131 *Pure appl. geophys.* 160, 1125–1136. <https://doi.org/10.1007/PL00012564>

1132 Takarli, M., Prince-Agbodjan, W., 2008. Temperature Effects on Physical Properties and Mechanical
1133 Behavior of Granite: Experimental Investigation of Material Damage. *JAI* 5, 1–13.
1134 <https://doi.org/10.1520/JAI100464>

1135 Tang, Z.C., Sun, M., Peng, J., 2019. Influence of high temperature duration on physical, thermal and
1136 mechanical properties of a fine-grained marble. *Applied Thermal Engineering* 156, 34–50.
1137 <https://doi.org/10.1016/j.applthermaleng.2019.04.039>

1138 Tarasovs, S., Ghassemi, A., 2012. On the role of thermal stress in reservoir stimulation. Proceedings:
1139 Thirty-Seventh Workshop on Geothermal Reservoir Engineering.
1140 Tian, W.-L., Yang, S.-Q., Elsworth, D., Wang, J.-G., Li, X.-Z., 2020. Permeability evolution and crack
1141 characteristics in granite under treatment at high temperature. *International Journal of Rock
1142 Mechanics and Mining Sciences* 134, 104461. <https://doi.org/10.1016/j.ijrmms.2020.104461>
1143 Ueda, A., Kato, K., Ohsumi, T., Yajima, T., Ito, H., Kaieda, H., Metcalfe, R., Takase, H., 2005.
1144 Experimental studies of CO₂-rock interaction at elevated temperatures under hydrothermal
1145 conditions. *Geochemical Journal* 39, 417–425. <https://doi.org/10.2343/geochemj.39.417>
1146 Vazquez, P., Carrizo, L., Thomachot-Schneider, C., Gibeaux, S., Alonso, F.J., 2016. Influence of surface
1147 finish and composition on the deterioration of building stones exposed to acid atmospheres.
1148 *Construction and Building Materials* 106, 392–403.
1149 <https://doi.org/10.1016/j.conbuildmat.2015.12.125>
1150 Vazquez, P., Sánchez-Delgado, N., Carrizo, L., Thomachot-Schneider, C., Alonso, F.J., 2018. Statistical
1151 approach of the influence of petrography in mechanical properties and durability of granitic
1152 stones. *Environ Earth Sci* 77, 287. <https://doi.org/10.1007/s12665-018-7475-6>
1153 Vazquez, P., Shushakova, V., Gómez-Heras, M., 2015. Influence of mineralogy on granite decay
1154 induced by temperature increase: Experimental observations and stress simulation.
1155 *Engineering Geology* 189, 58–67. <https://doi.org/10.1016/j.enggeo.2015.01.026>
1156 Vazquez, P., Siegesmund, S., Alonso, F.J., 2011. Bowing of dimensional granitic stones. *Environ Earth
1157 Sci* 63, 1603–1612. <https://doi.org/10.1007/s12665-010-0882-y>
1158 Vera, J.A., 2004. *Geología de España*. SGE-IGME.
1159 Weng, L., Wu, Z., Li, X., 2018. Mesodamage Characteristics of Rock with a Pre-cut Opening Under
1160 Combined Static–Dynamic Loads: A Nuclear Magnetic Resonance (NMR) Investigation. *Rock
1161 Mech Rock Eng* 51, 2339–2354. <https://doi.org/10.1007/s00603-018-1483-4>
1162 Wogelius, R.A., Milodowski, A.E., Field, L.P., Metcalfe, R., Lowe, T., van Veelen, A., Carpenter, G.,
1163 Norris, S., Yardley, B., 2020. Mineral reaction kinetics constrain the length scale of rock
1164 matrix diffusion. *Scientific Reports* 10, 8142. <https://doi.org/10.1038/s41598-020-65113-x>
1165 Wu, Q., Weng, L., Zhao, Y., Guo, B., Luo, T., 2019. On the tensile mechanical characteristics of fine-
1166 grained granite after heating/cooling treatments with different cooling rates. *Engineering
1167 Geology* 253, 94–110. <https://doi.org/10.1016/j.enggeo.2019.03.014>
1168 Xu, C., Sun, Q., 2018. Effects of quenching cycle on tensile strength of granite. *Géotechnique Letters*
1169 8, 165–170. <https://doi.org/10.1680/jgele.18.00053>
1170 Xu, X., Gao, F., Shen, X., Xie, H., 2008. Mechanical characteristics and microcosmic mechanisms of
1171 granite under temperature loads. *Journal of China University of Mining and Technology* 18,
1172 413–417. [https://doi.org/10.1016/S1006-1266\(08\)60086-3](https://doi.org/10.1016/S1006-1266(08)60086-3)
1173 Yilmaz, N., Karaca, Z., Goktan, R.M., Akal, C., 2009. Relative brittleness characterization of some
1174 selected granitic building stones: Influence of mineral grain size. *Construction and Building
1175 Materials* 23, 370–375. <https://doi.org/10.1016/j.conbuildmat.2007.11.014>
1176 Yong, C., Wang, C., 1980. Thermally induced acoustic emission in westerly granite. *Geophysical
1177 Research Letters* 7, 1089–1092. <https://doi.org/10.1029/GL007i012p01089>
1178 Yu, P., Pan, P.-Z., Feng, G., Wu, Z., Zhao, S., 2020. Physico-mechanical properties of granite after
1179 cyclic thermal shock. *Journal of Rock Mechanics and Geotechnical Engineering* 12, 693–706.
1180 <https://doi.org/10.1016/j.jrmge.2020.03.001>
1181 Yun, T.S., Jeong, Y.J., Kim, K.Y., Min, K.-B., 2013. Evaluation of rock anisotropy using 3D X-ray
1182 computed tomography. *Engineering Geology* 163, 11–19.
1183 <https://doi.org/10.1016/j.enggeo.2013.05.017>
1184 Zeng, Y., Tang, L., Wu, N., Cao, Y., 2017. Analysis of influencing factors of production performance of
1185 enhanced geothermal system: A case study at Yangbajing geothermal field. *Energy* 127, 218–
1186 235. <https://doi.org/10.1016/j.energy.2017.03.100>

- 1187 Zhang, F., Zhao, J., Hu, D., Skoczylas, F., Shao, J., 2018. Laboratory Investigation on Physical and
1188 Mechanical Properties of Granite After Heating and Water-Cooling Treatment. *Rock Mech*
1189 *Rock Eng* 51, 677–694. <https://doi.org/10.1007/s00603-017-1350-8>
- 1190 Zhang, W., Sun, Q., Zhang, Y., Xue, L., Kong, F., 2018. Porosity and wave velocity evolution of granite
1191 after high-temperature treatment: a review. *Environ Earth Sci* 77, 350.
1192 <https://doi.org/10.1007/s12665-018-7514-3>
- 1193 Zhao, Yangsheng, Feng, Z., Zhao, Yu, Wan, Z., 2017. Experimental investigation on thermal cracking,
1194 permeability under HTHP and application for geothermal mining of HDR. *Energy* 132, 305–
1195 314. <https://doi.org/10.1016/j.energy.2017.05.093>
- 1196 Zhou, C., Remoroza, A.I., Shah, K., Doroodchi, E., Moghtaderi, B., 2016. Experimental study of static
1197 and dynamic interactions between supercritical CO₂/water and Australian granites.
1198 *Geothermics* 64, 246–261. <https://doi.org/10.1016/j.geothermics.2016.05.007>
- 1199 Zhu, Z., Tian, H., Chen, J., Jiang, G., Dou, B., Xiao, P., Mei, G., 2020. Experimental investigation of
1200 thermal cycling effect on physical and mechanical properties of heated granite after water
1201 cooling. *Bull Eng Geol Environ* 79, 2457–2465. <https://doi.org/10.1007/s10064-019-01705-w>
1202